

**A UNIFIED VISCOELASTO-PLASTIC DAMAGE MODEL FOR LONG-TERM
PERFORMANCE OF PRESTRESSED CONCRETE BOX GIRDERS**

by

Jie Zhang

B.S. in Engineering, South China Agricultural University, 2013

Submitted to the Graduate Faculty of
Swanson School of Engineering in partial fulfillment
of the requirements for the degree of
Master of Science

University of Pittsburgh

2015

UNIVERSITY OF PITTSBURGH
SWANSON SCHOOL OF ENGINEERING

This thesis was presented

by

Jie Zhang

It was defended on

June 5, 2015

and approved by

Qiang Yu, PhD, Assistant Professor

Morteza Torkamani, PhD, Associate Professor

Jeen-Shang Lin, PhD, Associate Professor

Thesis Advisor: Qiang Yu, PhD, Assistant Professor

Copyright © by Jie Zhang

2015

**A UNIFIED VISCOELASTO-PLASTIC DAMAGE MODEL FOR LONG-TERM
PERFORMANCE OF PRESTRESSED CONCRETE BOX GIRDERS**

Jie Zhang, M.S.

University of Pittsburgh, 2015

The prediction of long-term deflection of large-span prestressed concrete bridges is a serious challenge to the current progress towards sustainable transportation system, which requires for a longer service lifetime. Although a number of concrete models and numerical formulations were proposed, the accuracy of prediction is not satisfactory and significant underestimate happens in structural analysis.

In order to overcome this obstacle, a unified viscoelasto-plastic damage model is proposed for the prediction of long-term performance of large-span prestressed concrete bridges carrying heavy traffic flow. In this unified concrete model, concrete cracking, plasticity and history-dependent behaviors (e.g. static creep, cyclic creep and shrinkage) are coupled. The isotropic damage model developed by Tao and Phillips enriched with the plastic yield surface is used in this study. For the static creep and shrinkage models, the rate-type formulation is applied so as to 1) save the computational cost and 2) make it admissible to couple memory-dependent and -independent processes. Cyclic creep, which is frequently ignored in structural analysis, is found to contribute substantially to the deflections of bridges with heavy traffic loads. The model is embedded in the general FEM program ABAQUS and a case study is carried out on the Humen Bridge Auxiliary Bridge. The simulation results are compared to the inspection reports, and the effectiveness of the proposed model is supported by the good agreement between the simulation and in-situ measurements.

TABLE OF CONTENTS

PREFACE.....	X
1.0 INTRODUCTION.....	1
2.0 FRAMEWORK FOR UNIFIED MODEL	7
3.0 VISCOELASTO-PLASTIC DAMAGE MODEL.....	10
3.1 ISOTROPIC DAMAGE VARIABLE.....	10
3.2 PLASTIC PART	13
3.3 CONSISTENT THERMODYNAMIC EQUATION.....	15
3.3.1 Elastic part of Helmholtz free energy	17
3.3.2 Plastic part of Helmholtz free energy	18
3.4 CONSISTENCY CONDITIONS	19
3.4.1 Plastic consistency condition.....	19
3.4.2 Damage consistency condition.....	20
4.0 MEMORY-DEPENDNT BEHAVIOR.....	22
4.1 STATIC CREEP	22
4.2 CYCLIC CREEP	25
4.3 SHRINKAGE.....	28
5.0 NUMERICAL IMPLEMENTAION.....	30
5.1 GENERAL IMPLEMENTATION	30

5.2	CALCULATION OF THE PLASTIC MULTIPLIER	33
5.3	EVOLUTION OF THE DAMAGE VARIABLES	35
5.4	OVERALL FLOWCHART	37
6.0	CASE STUDY	40
6.1	BRIDGE INTRODUCTION.....	40
6.1.1	Specific dimension	41
6.1.2	Traffic investigation	43
6.2	FINITE ELEMENT MODEL	48
6.3	SIMULATION APPROACH	50
6.4	SIMULATION RESULTS.....	52
6.4.1	The pure viscoelastic analysis.....	52
6.4.2	The unified model	56
6.5	CRACK AND DAMAGE DISTRIBUTION	60
7.0	CONCLUSION.....	64
	APPENDIX A	66
	APPENDIX B	68
	BIBLIOGRAPHY	70

LIST OF TABLES

Table 1. Vehicle classification.....	45
--------------------------------------	----

LIST OF FIGURES

Figure 1. The unified viscoelasto-plastic damage and memory-dependent model.....	9
Figure 2. Kelvin chain model.....	23
Figure 3. The overall flowchart of the numerical implementation based on the unified model by ABAQUS	37
Figure 4. The flowchart of return mapping algorithm	38
Figure 5. The flowchart of damage variable calculation	39
Figure 6. Humen Bridge Auxiliary Channel Bridge.....	41
Figure 7. The dimension of cross-section at the pier (mm)	42
Figure 8. The dimension of cross-section at the middle span (mm).....	43
Figure 9. Traffic volume from 1998 to 2010	44
Figure 10. The volume proportion of the six types in 1998.....	45
Figure 11. The volume proportion of the six types in 1999.....	46
Figure 12. The volume proportion of the six types in 2000.....	46
Figure 13. The volume proportion of the six types in 2001.....	47
Figure 14. The volume proportion of the six types in 2002.....	47
Figure 15. The volume of type 6 vehicles from 1998 to 2002.....	48
Figure 16. ABAQUS model for the Humen Bridge	49
Figure 17. The detailed distribution of prestressing tendons	50

Figure 18. The deflection at the middle point for pure viscoelastic analysis with linear time scale	53
Figure 19. The deflection at the middle point for pure viscoelastic analysis with log time scale	53
Figure 20. The comparison of deflections at middle point from measurements and simulations based on pure viscoelastic analysis models in 7 years with linear time scale	55
Figure 21. The comparison of deflections at middle point from measurements and simulations based on pure viscoelastic analysis models in 7 years with log time scale	55
Figure 22. The comparison of deflections at middle point based on measurements and simulations from the unified models in 7 years with linear time scale.....	57
Figure 23. The comparison of deflections at middle point based on measurements and simulations from the unified models in 7 years with log time scale.....	57
Figure 24. The first year profile from the unified model with B4 model and real measurements	58
Figure 25. The second year profile from the unified model with B4 model and real measurements	59
Figure 26. The third year profile from the unified model with B4 model and real measurements	59
Figure 27. The fourth year profile from the unified model with B4 model and real measurements	60
Figure 28. The fifth year profile from the unified model with B4 model and real measurements	60
Figure 29. The real crack distribution of Humen Bridge at 2003	61
Figure 30. The cracks and damage simulation based on the unified model by the end of construction.....	62
Figure 31. The cracks and damage simulation based on the unified model after 1 year	62
Figure 32. The cracks and damage simulation based on the unified model after 3 years	63
Figure 33. The cracks and damage simulation based on the unified model after 7 years	63

PREFACE

First, I would like to thank my advisor Dr. Yu for providing me the opportunity to do the research and supporting me throughout my graduate studies. I could not finish my thesis without his instruction and education.

I would also like to acknowledge my committee members, Dr. Morteza Torkamani and Dr. Jeen-Shang Lin. Thank you for your precious time and wise advice.

Furthermore, I would like to extend my gratitude and appreciation to Tong Teng, the PhD student of Dr. Yu, for helping me in the theoretical knowledge study and guiding me with the simulation.

Moreover, I would like to thank Chunlin Pan and Weijing Wang, the PhD students of Dr. Yu, for their precious advices on my thesis.

Finally, I would like to take this opportunity to express my thanks to my parents for their continuous support throughout my graduate studies.

1.0 INTRODUCTION

To realistically predict the long-term behavior of a large-span prestressed concrete bridge is a serious challenge to the current progress towards sustainable transportation system, which requires for a longer service lifetime. According to a recent survey (Bažant et al., 2012 a,b), a great number of bridges worldwide are suffering the excessive deflections which were significantly underestimated in design. The unexpected deflection will result in cracks in concrete members, and therefore significantly compromise the safety and serviceability of a prestressed concrete bridge. For example, the Koror-Babeldaob (KB) bridge with a large-span of 241 m, developed an excessive deflection and collapsed in 1996, three months after remedial work (Bažant et al., 2010, 2012 a,b). Based on the design with CEB-fib recommendation (Comité Euro-International du Béton, 1972), the final deflection from the design camber (0.3 m) should be terminated at 0.76-0.88 m. According to the ACI recommendation (American Concrete Institute, 1971), the deflection from the design camber should be 0.71 m (McDonald et al., 2003) and 0.737 (Bažant et al., 2012 a,b). However, a year before the collapse, the deflection of KB Bridge already developed to 1.39 m from camber and kept evolving (Bažant et al., 2012 a,b). In addition, an extra creep deflection had accumulated during construction which caused a reduction of the camber from the design

value 0.3 m to only 0.075 m. Therefore the total deflection in 1995 was 1.61m (Bažant et al., 2012 a,b), which was more than double of the design deflection.

One reason for the underestimate in design was the obsolete material model (Yu et al., 2012, Bažant et al., 2012 a,b, Wendner et al., in press a,b). Both the CEB-fib recommendation, which is an old version of fib MC2010 (Fédération Internationale du Béton, 2012), and the ACI recommendation used in design gave inaccurate predictions about the long-term creep and shrinkage, which are the two major causes of the deflection. To improve the accuracy, B3 model, which is an old version of B4 model (Bažant et al., in press), was developed by Bažant and Baweja (2000). The B3 model and B4 model not only match the experimental data better, but are also easier to be theoretically justified than the ACI and CEB-FIP model (Hubler et al., 2015, Wendner et al., in press a,b). The creeps in B3 Model (Bažant and Baweja, 2000) and B4 model (Bažant et al., in press) are divided into basic creep and drying creep based on the solidification theory (Bažant and Prasannan 1989 a,b, Bažant and Baweja 2000). The basic creep is unbounded and consists of short-term strain, viscous strain and a flow term while the drying creep is bounded and related to moisture loss. In addition, the parameters in B3 and B4 model are adjustable which can be updated according to the experiment data and the material used in bridge (Bažant et al., 2011). The simulations of KB Bridge based on the B3 model and other previous models were done by Bažant et al. (2012 a,b), the results of which prove that predicted deflection by B3 model with suitable parameters is more realistic than the rest and matches the real deflection quite well. To further prove the effectiveness of B3 model, Bažant et al. also simulated the Konaru Bridge,

Urado Bridge, Koshirazu Bridge and Tsukiyono Bridge based on this model in 2012, and all the predictions are acceptable compared with the real measurements. The above simulations illustrate that with the appropriate parameters, B3 model can capture the deflection of a large-span bridge quite well with its accurate prediction in creep and shrinkage compared to the ACI and CEB-fib model. However, when a large-span prestressed concrete bridge is carrying heavy traffic flow, whether the pure viscoelastic analyses based on ACI, CEB-fib and B3 model can accurately predict the long-term deflection is still unknown. This stems from the fact that the influences of other factors, like damage, plasticity, and cyclic creep, remain poorly understood when heavy traffic flow is under consideration. If these influences are non-negligible, which will be proved true in this study, the pure viscoelastic analysis may not be able to accurately predict the deflection of a large-span prestressed concrete bridge with heavy traffic load.

Another cause for the underestimate of deflection is the analysis method. In the past, one-dimensional beam-type analysis was utilized to simulate the box girder with the approximate formulations of shear lag for the top slab. This method, common in commercial design software, however, has two deficiencies (Yu et al., 2012). One deficiency is that this method cannot accurately simulate the shear lag effects because they are both elastic and aging viscoelastic. Besides, these effects occur both in top/bottom slab and web and are caused by not only the shear forces from piers but also the concentrated loads by anchors. The other one is that beam-type analysis cannot take differences of drying creep and shrinkage caused by different factors into account. Therefore, a three dimensional finite

element analysis is utilized where the box girder is considered as a thick shell (Yu et al., 2012). Because the stress obtained from the principle of superposition follows a linearly viscoelastic stress-strain relation in Volterra integral form, the creep can be calculated by using Volterra integral equations in the three dimensional finite element analysis, which is called integral-type method and is very popular now (Yu et al., 2012). However, this integral-type implementation method is not fit for this study because it has two disadvantages. The first one is that all the previous data like strain need to be stored to proceed current simulation, which will cause a huge computational cost. The second one is that this implementation is not compatible with many memory-independent phenomena, like damage and plasticity (Yu et al., 2012).

To mitigate the underestimate of deflection, a viscoelasto-plastic unified concrete model with memory-dependent and -independent behaviors (note as “the unified model” hereafter) is developed in this study. In this new unified model, the creep and shrinkage models, like ACI (American Concrete Institute Committee, 2008), fib MC 2010 (Fédération Internationale du Béton, 2012) and B4 model (Bažant et al., in press) are selected in pure viscoelastic analysis. In addition, the unified model also takes other memory-dependent and -independent phenomena, like damage, plasticity and cyclic creep into account in order to improve the prediction accuracy for the long-term behavior of a large-span prestressed concrete bridge with heavy traffic flow. Instead of the integral-type, the rate-type implementation with exponential algorithm is utilized in this study which can overcome the two disadvantages from the integral-type mentioned above (Yu et al., 2012, Bažant et al.,

2012, Wendner et al., in press a,b). In the rate-type algorithm, the viscoelastic stress-strain relation can be approximated by a rheological model (e.g. Kelvin chain model, Maxwell chain model) (Yu et al., 2012). Kelvin chain model is selected in this study which consists of a series of Kelvin chain units with coupled spring and dashpot. In rate-type implementation, by transferring the incremental stress-strain relation to a quasi-elastic incremental stress-strain relation, the creep calculation can be simplified to a series of elasticity problems with initial strains (Jir ásek and Bažant, 2002, Yu et al., 2012). Because of this simplification, the storage of previous data is no more necessary and the computational cost can be greatly reduced, which is important to the large-scale structure analysis. In addition, this transformation makes it convenient for one to couple the creep and shrinkage and other factors like steel relaxation, cyclic, damage, and plasticity.

To avoid the tragedy like KB Bridge and many other collapsed bridges again, a more comprehensive and effective concrete model is necessary. Yet, limited concrete model combining the damage, plasticity and the memory-dependent behaviors (e.g. static creep, cyclic creep, shrinkage, etc.) is available now and barely any research is focusing on it. Therefore, the objective of this study is to propose a comprehensive concrete model coupling the damage, plasticity and the memory-dependent behaviors to accurately predict the long-term deflection of the large-span prestressed concrete bridge especially for those carrying heavy traffic. In this study, both the pure viscoelastic analysis and the unified model will be implemented by the finite element software ABAQUS to simulate Humen Bridge Auxiliary Channel Bridge (denoted as “Humen Bridge” hereafter), a large-span prestressed concrete

bridge with heavy traffic load. The simulation results will be compared with the real deflections of the bridge in order to verify the effectiveness of this unified model.

The rest part of this thesis is arranged in the following style. Following the introduction of the background of the concrete models and analysis methods and the significance of the new effective concrete model, in the Chapter 2, the general framework of the unified concrete models is demonstrated. Then Chapter 3 focuses on the damage and plasticity behaviors and their thermodynamic consistency conditions. Chapter 4 introduces mainly the three memory-dependent behaviors, static creep, cyclic creep and shrinkage. The numerical implementation is illustrated in Chapter 5 with three flowcharts. A case study about the simulation of Humen Bridge is described in the Chapter 6, where the finite element model and the simulation method are displayed, followed by the comparison and discussion. At last, conclusions of this thesis is drawn in Chapter 7.

2.0 FRAMEWORK FOR UNIFIED MODEL

In this study, the unified model is proposed where the instantaneous behavior and memory-dependent behavior are considered. Therefore, the total strain tensor ε_{ij} can be decomposed into the instantaneous strain tensor ε_{ij}^i and the memory-dependent strain tensor ε_{ij}^t . The instantaneous strain tensor, including the elastic strain tensor ε_{ij}^e and plastic strain tensor ε_{ij}^p , will develop instantaneously after loading, while the memory-dependent strain tensor ε_{ij}^t , including static creep ε_{ij}^{sc} , cyclic creep ε_{ij}^{cc} and shrinkage ε_{ij}^{sh} , will grow with the time. The mathematical expression for the decomposition is expressed as:

$$\varepsilon_{ij} = \underbrace{(\varepsilon_{ij}^e + \varepsilon_{ij}^p)}_{\varepsilon_{ij}^i} + \underbrace{(\varepsilon_{ij}^{sc} + \varepsilon_{ij}^{cc} + \varepsilon_{ij}^{sh})}_{\varepsilon_{ij}^t} \quad (\text{Eq. 2-1})$$

The one-dimensional illustration for the unified model is shown in Figure 1. The whole unified model can be separated into the following parts with the implementation sequence:

1. Due to the fatigue growth of pre-existing microcracks in hydrated cement, cyclic creep is developed which can be calculated by the mathematical algorithm developed by the Bažant and Hubler (2014).

2. The variation of humidity and temperature will lead to the shrinkage which is calculated based on the shrinkage models.

3. The static creep is calculated based on the rate-type algorithm, where the viscoelastic part is approximated by a series of Kelvin chain model. In rate-type implementation, the creep calculation can be simplified to a series of elasticity problems with initial strains by transferring the incremental stress-strain relation to a quasi-elastic incremental stress-strain relation (Jir ásek and Bažant, 2002, Yu et al., 2012).

4. Then, the plastic part can be isolated by the return mapping algorithm (Simo and Hughes, 1998) from the rest parts, which is convenient for one to calculate the plastic strain. Whether the plastic strain remains or evolves is determined by the plasticity consistency conditions.

5. Next, the elastic part is calculated, which is governed by the spring with the Yong's modulus $E(t)$ which is a function of the age t of concrete (Bažant and Prasannan, 1989 a,b).

6. The damage part is considered at last. Similar to the plasticity, damage remains when the principal stress within the damage surface, and evolves when the principal stress violate the damage criterion. The damage is realized by degradation of the stiffness matrix of spring and of the Kelvin chain units.

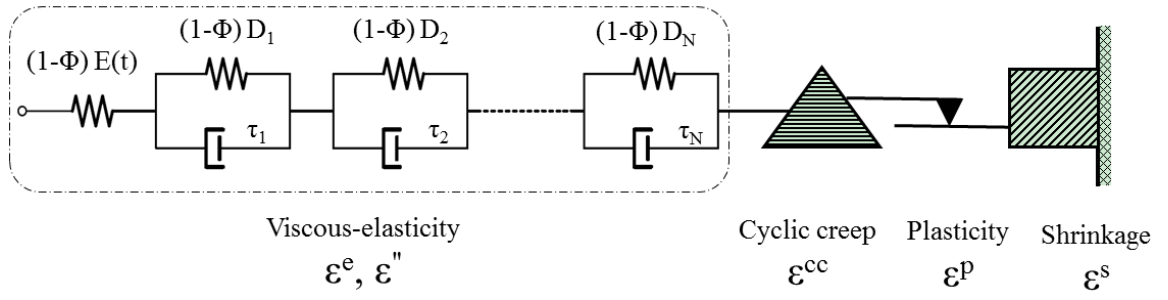


Figure 1. The unified viscoelasto-plastic damage and memory-dependent model

3.0 VISCOELASTO-PLASTIC DAMAGE MODEL

3.1 ISOTROPIC DAMAGE VARIABLE

The damage model in this study is derived according to the isotropic damage theory. This model is thermodynamically consistent and small strains and isothermal conditions are assumed here.

In this model, the damaged configuration is transformed from the effective (undamaged) one. This can be realized through either strain equivalence or strain energy equivalence hypothesis (Voyiadjis and Kattan, 2006). In this study, strain equivalence hypothesis is utilized which assumes that the strain tensors in the damaged configuration are equivalent to those in the effective (undamaged) configuration. Because this hypothesis is generally applied to couple the plasticity and continuum damage behaviors (Menzel et al., 2005; Voyiadjis and Kattan, 2006), the plastic strain tensor ε_{ij}^p , elastic strain tensor ε_{ij}^e and the instantaneous strain tensor $\varepsilon_{ij}^i = \varepsilon_{ij}^p + \varepsilon_{ij}^e$ are considered here. Therefore, the hypothesis can be expressed as:

$$\begin{cases} \mathcal{E}_{ij}^e = \bar{\mathcal{E}}_{ij}^e \\ \mathcal{E}_{ij}^p = \bar{\mathcal{E}}_{ij}^p \\ \mathcal{E}_{ij}^i = \bar{\mathcal{E}}_{ij}^i \end{cases} \quad (\text{Eq. 3-1})$$

Then by utilizing the Hook's law, the effective (undamaged) stress tensor $\bar{\sigma}_{ij}$ can be obtained as:

$$\bar{\sigma}_{ij} = \bar{E}_{ijkl}(t) \bar{\mathcal{E}}_{kl}^e = \bar{E}_{ijkl}(t) \mathcal{E}_{kl}^e \quad (\text{Eq. 3-2})$$

where $\bar{E}_{ijkl}(t)$ is the fourth-order effective (undamaged) isotropic elasticity tensor, which is a function of the age t of concrete. For the linear elastic materials, $\bar{E}_{ijkl}(t)$ is given as:

$$\bar{E}_{ijkl}(t) = 2\bar{G}(t)I_{ijkl}^{dev} + \bar{K}(t)\delta_{ij}\delta_{kl} \quad (\text{Eq. 3-3})$$

where $I_{ijkl}^{dev} = I_{ijkl} - \frac{1}{3}\delta_{ij}\delta_{kl}$ is the deviatoric part of the fourth-order identity tensor $I_{ijkl} = 0.5(\delta_{ik}\delta_{jl} + \delta_{il}\delta_{jk})$. $\bar{G}(t)$ and $\bar{K}(t)$ are the effective (undamaged) shear and bulk moduli, respectively. The tensor δ_{ij} is the Kronecker delta calculated as:

$$\begin{cases} \delta_{ij} = 1 & \text{when } i = j \\ \delta_{ij} = 0 & \text{when } i \neq j \end{cases} \quad (\text{Eq. 3-4})$$

The stress in damaged configuration can be written as:

$$\sigma_{ij} = E_{ijkl}(t) \mathcal{E}_{kl}^e \quad (\text{Eq. 3-5})$$

where $E_{ijkl}(t)$ is the fourth-order damaged isotropic elasticity tensor.

In isotropic damage model, a scalar (isotropic) damage variable Φ , which represents the average crack density, is introduced to transform an undamaged stress tensor into a damaged one. This transformation is defined as:

$$\sigma_{ij} = (1 - \Phi)\bar{\sigma}_{ij} = (1 - \Phi)\bar{E}_{ijkl}(t) \mathcal{E}_{ij}^e \quad (\text{Eq. 3-6})$$

By substituting Eq. 3-6 into Eq. 3-2, the relation between the fourth-order isotropic elasticity tensor in undamaged configuration $\bar{E}_{ijkl}(t)$ and in damaged configuration $E_{ijkl}(t)$ can be obtained as:

$$E_{ijkl} = (1 - \Phi) \bar{E}_{ijkl} \quad (\text{Eq. 3-7})$$

To account for the different effects of damage mechanisms on the nonlinear performance of concrete, the Cauchy stress tensor can be decomposed into tensile stress tensor σ_{ij}^+ and compressive stress tensor σ_{ij}^- by spectral decomposition (Ortiz, 1985; Lubliner et al., 1989; Lee and Fenves, 1998; Wu et al., 2006) as:

$$\sigma_{ij} = \sigma_{ij}^+ + \sigma_{ij}^- \quad (\text{Eq. 3-8})$$

The total Cauchy stress tensor can be calculated by the combination of the principal values and their principal directions as:

$$\sigma_{ij} = \sum_{k=1}^3 \hat{\sigma}^{(k)} n_i^{(k)} n_j^{(k)} \quad (\text{Eq. 3-9})$$

According to Eq. 3-9, the tension part can be calculated by only combining tensile principal values with their directions like:

$$\sigma_{ij}^+ = \sum_{k=1}^3 H(\hat{\sigma}^{(k)}) \hat{\sigma}^{(k)} n_i^{(k)} n_j^{(k)} \quad (\text{Eq. 3-10})$$

where the $H(\hat{\sigma}^{(k)})$ is called Heaviside step function that $H(\hat{\sigma}^{(k)}) = 1$ when $\hat{\sigma}^{(k)} > 0$ and $H(\hat{\sigma}^{(k)}) = 0$ when $\hat{\sigma}^{(k)} < 0$.

In the same way, the compression part of Cauchy stress tensor σ_{ij}^- can also be calculated by combining compression principal values with their directions.

Then, the dimensionless scalar damage variable Φ is defined (Tao and Phillips, 2005) as:

$$\Phi = \frac{\|\sigma_{ij}^+\| \Phi^+ + \|\sigma_{ij}^-\| \Phi^-}{\|\sigma_{ij}\|} \quad (\text{Eq. 3-11})$$

where Φ^+ , Φ^- are tensile and compressive damage variables, respectively. $\|\sigma_{ij}\|$ represents the scalar contraction of the second order tensor, i.e. $\|\sigma_{ij}\| = \sigma_{ij} \sigma_{ij}$. This damage variable is adopted in this study because it can take both tension and compression into consideration .

3.2 PLASTIC PART

In plasticity theory, the yield surface (criterion) of the model is always a key property. This surface should accurately model the non-symmetrical behavior when concrete is under both tensile and compressive external forces. In this study, the yield surface is developed by the Lubliner et al. (1989) and adapted by Lee and Fenves (1998) and Wu et al. (2006). This surface can successfully simulate the concrete behaviors under uniaxial, biaxial, multiaxial and repeated loadings and is expressed as:

$$f = \sqrt{3\bar{J}_2} + \alpha\bar{I}_1 + \beta(\kappa^\pm)H(\hat{\sigma}_{\max})\hat{\sigma}_{\max} - (1-\alpha)c^-(\kappa^-) \leq 0 \quad (\text{Eq. 3-12})$$

where $\bar{J}_2 = \bar{s}_{ij}\bar{s}_{ij}/2$ is the second-invariant of the effective deviatoric stress and $\bar{s}_{ij} = \bar{\sigma}_{ij} - \bar{\sigma}_{kk}\delta_{ij}/3$. $\bar{I}_1 = (\bar{\sigma}_{ii})/3$ is the first-invariant of the effective stress tensor $\bar{\sigma}_{ij}$. $H(\hat{\sigma}_{\max})$ is the Heaviside step function, the same operation as in damage part (Eq. 3-10), and $\hat{\sigma}_{\max}$ is the maximum principle effective stress. κ^\pm are the hardening parameters under tension and compression respectively and calculated as (Lee and Fenves, 1998):

$$\kappa^\pm = \int_0^t \dot{\kappa}^\pm dt \quad (\text{Eq. 3-13})$$

where $\dot{\kappa}^{\pm}$ are the equivalent plastic strain rates. The tensile rate $\dot{\kappa}^+$ and compressive rate $\dot{\kappa}^-$ can be calculated separately by expressions (Lee and Fenves, 1998) as:

$$\dot{\kappa}^+ = r(\hat{\sigma}_{ij}) \hat{\epsilon}_{\max}^p \quad (\text{Eq. 3-14})$$

$$\dot{\kappa}^- = -(1 - r(\hat{\sigma}_{ij})) \hat{\epsilon}_{\min}^p \quad (\text{Eq. 3-15})$$

$\hat{\epsilon}_{\max}^p$ and $\hat{\epsilon}_{\min}^p$ are the maximum and minimum eigenvalues of the plastic strain rate tensor. It should be noted here that the function to calculate eigenvalues and their directions of a certain second-order tensor like stress or strain tensor is available in user-subroutine UMAT in ABAQUES, which is convenient for one to obtain the $\hat{\epsilon}_{\max}^p$ and $\hat{\epsilon}_{\min}^p$. By this function, the principle stresses $\hat{\sigma}^{(k)}$ and their directions can also be easily obtained. The dimensionless parameter $r(\hat{\sigma}_{ij})$ in Eq. 3-14 and Eq. 3-15 is a weight factor of principle stresses $\hat{\sigma}_{ij}$ and is defined as (Lee and Fenves, 1998):

$$r(\hat{\sigma}_{ij}) = \frac{\sum_{k=1}^3 \langle \hat{\sigma}_k \rangle}{\sum_{k=1}^3 |\hat{\sigma}_k|} \quad (\text{Eq. 3-16})$$

where $\langle \cdot \rangle$ is calculated as $\langle x \rangle = \frac{1}{2}(|x| + x)$. Note that the range of this weight factor should be $0 \leq r(\hat{\sigma}_{ij}) \leq 1$. When all the eigenstresses $\hat{\sigma}_{ij}$ are positive, the weight factor equals one and when all the eigenstresses $\hat{\sigma}_{ij}$ are negative, it equals zero.

The parameter α in Eq. 3-12 is a dimensionless constant developed by Lubliner et al. (1989) and is expressed as:

$$\alpha = \frac{(f_{b0}^- / f_0^-) - 1}{2(f_{b0}^- / f_0^-) - 1} \quad (\text{Eq. 3-17})$$

f_{b0}^- is the initial biaxial compressive yield stress and f_0^- is the uniaxial one. Generally, α is assumed from 0.08 to 0.14 according to experiments (Lubliner et al., 1989). The parameter β in Eq. 3-12 is developed by Lee and Fenves in 1998 and given as:

$$\beta(\kappa^\pm) = (1-\alpha) \frac{c^-(\kappa^-)}{c^+(\kappa^+)} - (1+\alpha) \quad (\text{Eq. 3-18})$$

$c^+(\kappa^+)$ and $c^-(\kappa^-)$ are the cohesion parameters which will be calculated in section 3.3.2.

3.3 CONSISTENT THERMODYNAMIC EQUATION

The Helmholtz free energy of concrete is generally a combination of elastic, plastic and damage behaviors (Tao and Phillips, 2005). According to the hypothesis of uncoupled elasticity (Lubliner, 1989, Wu et al., 2006), the unit volume of free energy ψ can be decomposed into the elastic part ψ^e and the plastic part ψ^p . In this study, the elastic strain tensor ε_{ij}^e and damage variables Φ^+ , Φ^- are considered in the elastic part of free energy while the plastic hardening variables κ^+ , κ^- are considered in the plastic part. Therefore, the unit volume of Helmholtz free energy can be expressed as (Taqieddin, 2008):

$$\psi = \psi^e(\varepsilon_{ij}^e, \Phi^+, \Phi^-) + \psi^p(\kappa^+, \kappa^-) \quad (\text{Eq. 3-19})$$

Because the isothermal condition is assumed here, the second-law of thermodynamics can be applied. It states that the rate change of internal energy should be no more than the external expenditure power. According to this law, the following relation can be obtained:

$$\int_v \rho \dot{\psi} dv \leq P_{ext} \quad (\text{Eq. 3-20})$$

where P_{ext} can be calculated by the principle of virtual work:

$$P_{ext} = P_{int} = \int_v \sigma_{ij} \dot{\varepsilon}_{ij} dv \quad (\text{Eq. 3-21})$$

By substituting Eq. 3-21 into Eq. 3-20, the following inequality can then be obtained:

$$(\sigma_{ij} \dot{\varepsilon}_{ij} - \rho \dot{\psi}) \geq 0 \quad (\text{Eq. 3-22})$$

where $\dot{\psi}$ is the rate of change in free energy and can be calculated by taking the time derivative of Eq. 3-19 as:

$$\dot{\psi} = \dot{\psi}^e + \dot{\psi}^p = \frac{\partial \psi^e}{\partial \varepsilon_{ij}^e} \dot{\varepsilon}_{ij}^e + \frac{\partial \psi^e}{\partial \Phi^+} \dot{\Phi}^+ + \frac{\partial \psi^e}{\partial \Phi^-} \dot{\Phi}^- + \frac{\partial \psi^p}{\partial \kappa^+} \dot{\kappa}^+ + \frac{\partial \psi^p}{\partial \kappa^-} \dot{\kappa}^- \quad (\text{Eq. 3-23})$$

Substituting Eq. 3-23 back into Eq. 3-22, one will get the following relation:

$$\sigma_{ij} \dot{\varepsilon}_{ij}^p + (\sigma_{ij} - \rho \frac{\partial \psi^e}{\partial \varepsilon_{ij}^e}) \dot{\varepsilon}_{ij}^e - \rho \frac{\partial \psi^e}{\partial \Phi^+} \dot{\Phi}^+ - \rho \frac{\partial \psi^e}{\partial \Phi^-} \dot{\Phi}^- - \rho \frac{\partial \psi^p}{\partial \kappa^+} \dot{\kappa}^+ - \rho \frac{\partial \psi^p}{\partial \kappa^-} \dot{\kappa}^- \geq 0 \quad (\text{Eq. 3-24})$$

The Cauchy stresses tensor is defined as $\sigma_{ij} = \rho \frac{\partial \psi^e}{\partial \varepsilon_{ij}^e}$ here to simplify the above

equation because Eq. 3-24 is valid for any allowable internal variable (Taqieddin, 2008).

Then Eq. 3-24 can be rewritten as the following relation:

$$\sigma_{ij} \dot{\varepsilon}_{ij}^p + Y^+ \dot{\Phi}^+ + Y^- \dot{\Phi}^- - c^+ \dot{\kappa}^+ - c^- \dot{\kappa}^- \geq 0 \quad (\text{Eq. 3-25})$$

where Y^\pm are defined as the damage thermodynamic conjugate forces and expressed as (Taqieddin, 2008):

$$Y^\pm = -\rho \frac{\partial \psi^e}{\partial \Phi^\pm} \quad (\text{Eq. 3-26})$$

c^\pm are defined as the plasticity cohesion conjugate forces and expressed as (Taqieddin, 2008):

$$c^{\pm} = \rho \frac{\partial \psi^p}{\partial \kappa^{\pm}} \quad (\text{Eq. 3-27})$$

3.3.1 Elastic part of Helmholtz free energy

The total effective (undamaged) elastic free energy is calculated as:

$$\rho \bar{\psi}^e = \frac{1}{2} \bar{\varepsilon}_{ij}^e \bar{E}_{ijkl} \bar{\varepsilon}_{kl}^e = \frac{1}{2} \bar{\sigma}_{ij} \bar{\varepsilon}_{ij}^e \quad (\text{Eq. 3-28})$$

Similar to the transformation from an undamaged stress tensor into a damaged one, the damaged elastic free energy can be transformed from the effective (undamaged) one according to elastic strain equivalence hypothesis (Voyiadjis and Kattan, 2006):

$$\rho \psi^e = (1 - \Phi) \rho \bar{\psi}^e = \frac{1}{2} \varepsilon_{ij}^e E_{ijkl} \varepsilon_{kl}^e = \frac{1}{2} \sigma_{ij} \varepsilon_{ij}^e \quad (\text{Eq. 3-29})$$

According to Resende (1987), the susceptibility of damage evolution for concrete is different under hydrostatic load and deviatoric load. Therefore, Tao and Philips (2005) adapted the free energy function in Eq. 3-29 into the following expression:

$$\rho \psi^e = \frac{1}{2} (1 - \Phi) \varepsilon_{ij}^e \bar{E}_{ijkl} \varepsilon_{kl}^e + \frac{1}{2} (1 - \beta) \Phi \left(\frac{1}{3} \varepsilon_{mm}^e \right)^2 \delta_{ij} \bar{E}_{ijkl} \delta_{kl} \quad (\text{Eq. 3-30})$$

Then, the damage thermodynamic conjugate forces Y^{\pm} can be calculated by substituting Eq. 3-30 into Eq. 3-26 that:

$$Y^{\pm} = -\rho \frac{\partial \psi^e}{\partial \Phi^{\pm}} = \frac{1}{2} \frac{\|\bar{\sigma}_{ij}^{\pm}\|}{\|\bar{\sigma}_{ij}\|} \left\{ \varepsilon_{ij}^e \bar{E}_{ijkl} \varepsilon_{kl}^e - \frac{1}{9} (1 - \beta) (\varepsilon_{mm}^e)^2 \delta_{ij} \bar{E}_{ijkl} \delta_{kl} \right\} \quad (\text{Eq. 3-31})$$

where β in Eq. 3-30 and Eq. 3-31 is a dimensionless reduction factor developed by Tao and Philips (2005) to reduce the susceptibility from the hydrostatic loading, and is expressed as:

$$\beta = 1 - \frac{1}{1 + cY \exp(-d \cdot Y)} \quad (\text{Eq. 3-32})$$

c and d here are two material constants ensuring the calculation results match the experimental data.

3.3.2 Plastic part of Helmholtz free energy

The total plastic free energy is a function of the hardening parameters κ^+ and κ^- , which expressed as (Tao and Philips, 2005):

$$\rho\psi^p = f_0^+ \kappa^+ + \frac{1}{2} h (\kappa^+)^2 + f_0^- \kappa^- + Q \left[\kappa^- - \frac{1}{\omega} \exp(-\omega \kappa^-) \right] \quad (\text{Eq. 3-33})$$

$c^+(\kappa^+)$ and $c^-(\kappa^-)$ are the cohesion parameters which are functions of hardening parameters κ^+ and κ^- respectively. These cohesion parameters suggest the evolution of stresses caused by plastic hardening or softening under uniaxial tensile or compression loadings. Because the concrete behavior under compression is more ductile, the compressive cohesion parameter $c^-(\kappa^-)$ is defined according to an exponential law as (Lubliner et al., 1989):

$$c^-(\kappa^-) = \rho \frac{\partial \psi^p}{\partial \kappa^-} = f_0^- + Q [1 - \exp(-\omega \kappa^-)] \quad (\text{Eq. 3-34})$$

Q and ω are two material constants that can characterize the saturated status. As for tensile cohesion parameter $c^+(\kappa^+)$, it is expressed in linear form such that (Lubliner et al., 1989):

$$c^+(\kappa^+) = \rho \frac{\partial \psi^p}{\partial \kappa^+} = f_0^+ + h \kappa^+ \quad (\text{Eq. 3-35})$$

where f_0^+ is the uniaxial tensile yield stress and h is a material constant.

3.4 CONSISTENCY CONDITIONS

3.4.1 Plastic consistency condition

The connection between plastic flow direction and plastic strain rate can be obtained by flow rule. Associated flow rule and non-associated flow rule are two major kinds. In this study, a non-associated flow rule is applied, in which the yield surface f is not consistent with plastic potential F^P . This means the plastic flow direction is not perpendicular to the yield criterion. For the frictional material like concrete, this rule can increase the accuracy when modeling the volumetric expansion under compression (Taqieddin, 2008). According to Chen and Han (1988), by using the associated flow rule with the yield criterion f in Eq. 3-12, the expansion of concrete is usually underestimated, while by using the non-associated flow rule with plastic potential F^P , this problem can be overcome. Therefore, the plastic strain rate can be obtained based on a non-associated flow rule as:

$$\dot{\varepsilon}_{ij}^P = \dot{\lambda}_p \frac{\partial F^P}{\partial \bar{\sigma}_{ij}} \quad (\text{Eq. 3-36})$$

where $\dot{\lambda}_p$ is known as the plastic loading factor or known as the Lagrangian plasticity multiplier. The plastic potential F^P is provided by Lee and Fenves (1998) as:

$$F^P = \sqrt{3J_2} + \alpha^P \bar{I}_1 \quad (\text{Eq. 3-37})$$

and then

$$\frac{\partial F^P}{\partial \bar{\sigma}_{ij}} = \frac{3}{2} \frac{\bar{S}_{ij}}{\sqrt{3J_2}} + a^P \delta_{ij} \quad (\text{Eq. 3-38})$$

where a^P is the expansion constant ranging from 0.2 to 0.3 for concrete according to experiment (Lee and Fenves, 1998).

The consistency conditions are related to the plasticity surface f and its rate \dot{f} which is calculated by taking the time derivative of f . This consistency can be expressed as (Voyiadjis and Kattan, 1992):

$$\begin{aligned} \text{If } f < 0 & \quad \text{then } \dot{\lambda}_p = 0 \\ \text{If } f = 0 \text{ and } \dot{f} \leq 0 & \quad \text{then } \dot{\lambda}_p = 0 \\ \text{If } f = 0 \text{ and } \dot{f} > 0 & \quad \text{then } \dot{\lambda}_p > 0 \end{aligned} \quad (\text{Eq. 3-39})$$

3.4.2 Damage consistency condition

To study the damage consistency, damage surfaces g^\pm , for tension and compression loadings respectively, are developed by Tao and Phillips (2005) and introduced here. Similar to the form by La Borderie et al. (1992), these surfaces are two functions of the damage thermodynamic conjugate forces Y^\pm and the scalar damage parameters Φ^\pm are expressed as:

$$g^\pm = Y^\pm - Y_0^\pm - Z^\pm \leq 0 \quad (\text{Eq. 3-40})$$

where Y_0^\pm are tensile and compressive initial damage thresholds respectively. Z^\pm are tensile and compressive softening parameters that follow a power law (Tao and Phillips, 2005) as:

$$Z^\pm = \frac{1}{a^\pm} \left(\frac{\Phi^\pm}{1 - \Phi^\pm} \right)^{\frac{1}{b^\pm}} \quad (\text{Eq. 3-41})$$

a^\pm and b^\pm are four material constants from the uniaxial experiment.

In the principal stress space, a tensile or compressive stress can be within or on the damage surface. When within the surface, the damage criterion will not be violated even if the stress point is under loading condition, which means the isotropic damage variable keeps the current status. When the stress level arrive at the damage surface, two situations are possible. One is unloading or keeping the same loading, and isotropic damage variable keeps the current status. The other one is loading and the damage evolve and isotropic damage variable needs to be updated. This consistency can be express as (Voyiadjis and Kattan, 1992):

$$\begin{aligned}
 \text{If } g < 0 & \quad \text{then } \dot{\Phi} = 0 \\
 \text{If } g = 0 \text{ and } \dot{g} \leq 0 & \quad \text{then } \dot{\Phi} = 0 \\
 \text{If } g = 0 \text{ and } \dot{g} > 0 & \quad \text{then } \dot{\Phi} > 0
 \end{aligned}
 \tag{Eq. 3-42}$$

4.0 MEMORY-DEPENDENT BEHAVIOR

4.1 STATIC CREEP

When concrete is under a unit stress applied at time t' , the static creep at current time t is generally characterized by the compliance function $J(t, t')$. Traditionally, because the stress $\sigma(t)$ obtained from the principle of superposition follows a linearly viscoelastic stress-strain relation in Volterra integral form, the creep can be calculated by using Volterra integral equation as $\int_{t'}^t J(t, t') d\sigma$. However, this integral-type method has two disadvantages when analyze the large-scale creep-sensitive structures (Yu et al., 2012):

1. Because of the concrete ageing, the kernel of Volterra integral equation $J(t, t')$ is not convolutional. This means all history data need to be stored and sums of all previous steps need to be analyzed, which greatly enhance computational cost.

2. More strictly, the method is not compatible with many influencing phenomena such as cracking, damage, humidity temperature, cyclic creep and steel relaxation.

To avoid the above disadvantages, instead of integral-type, the rate-type method with exponential algorithm is applied in this study. In the rate-type algorithm, the linearly viscoelastic stress-strain relation can be transferred into a quasi-elastic one with the

application of a rheology model (Yu et al., 2012). In this study, Kelvin chain model is selected and illustrated in Figure 2.

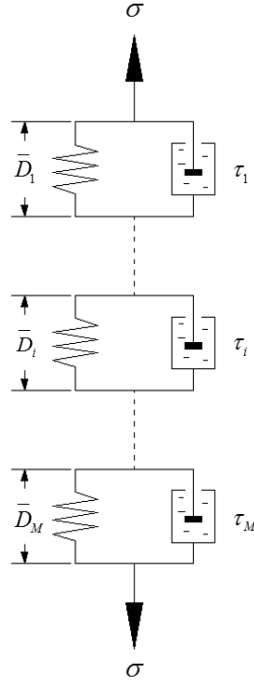


Figure 2. Kelvin chain model

This model consists of a series of kelvin chain units ($i = 1, 2, 3, \dots, M$) with the stiffness \bar{D}_i . With the retardation time τ_i , each unit couples a spring with the stiffness E_i and a dashpot with viscosity $\eta_i = E_i \tau_i$. For the 3-D rate-type formulation, incremental stress-strain relation is expressed as (Yu et al., 2012):

$$\Delta \bar{\sigma} = \bar{E}'' \Delta \varepsilon^e \quad (\text{Eq. 4-1})$$

where \bar{E}'' is the effective incremental modulus, which is given as:

$$\frac{1}{\bar{E}''} = \frac{1}{\bar{E}(t)} + \sum_{i=1}^M \bar{D}_i^{-1} \quad (\text{Eq. 4-2})$$

Next, the Kelvin chain unit stiffness \bar{D}_i and inelastic part of incremental static creep $\Delta\varepsilon''$ need to be calculated. The first can be achieved with the continuous retardation spectrum (Bažant, 1995) which provides a smoothed plot of compliance of kelvin chain units \bar{D}_i^{-1} against its retardation time τ_i in log scale. Then, by utilizing Laplace transformation inversion supplemented by Widder's approximate inversion formula (Widder, 1971), this spectrum can be identified uniquely with the given compliance function that (Bažant, 1995 and Yu et al., 2012):

$$L(\tau_i) = \frac{\lim_{k \rightarrow \infty} (k\tau_i)^k C^{(k)}(k\tau_i)}{(k-1)!} \quad (\text{Eq. 4-3})$$

The development of this continuous spectrum is shown in Appendix A. $C^{(k)}$ in Eq. 4-3 is the k -th order time derivative of the compliance function in creep part. In this study, $k = 3$ is accurate enough. Then with the discretization of the continuous spectrum, the discrete spectrum for each Kelvin unit can be obtained as (Bažant, 1995 and Yu et al., 2012):

$$A(\tau_i) = L(\tau_i) \ln 10 \quad (\text{Eq. 4-4})$$

To stabilize the implementation, the exponential algorithm (Appendix B) then is applied to obtain Kelvin chain unit stiffness \bar{D}_i with two internal state variables for each integration point in each step (Bažant et al., 1971 and 1975, Yu et al., 2012):

$$\beta_i = e^{-\Delta t / \tau_i} \quad (\text{Eq. 4-5})$$

$$\lambda_i = \tau_i (1 - \beta_i) / \Delta t \quad (\text{Eq. 4-6})$$

and then

$$\bar{D}_i = \frac{1}{A_i (1 - \lambda_i)} \quad (\text{Eq. 4-7})$$

The static creep increment $\Delta\varepsilon^{sc}$ can also be derived by this algorithm as (Yu et al., 2012):

$$\Delta\varepsilon'' = \sum_{i=1}^M \gamma_i^n (1 - \beta_i) \quad (\text{Eq. 4-8})$$

where γ_i^n is the internal state variable from the last time increment, which can be updated after obtaining the effective stress increment as (Yu et al., 2012):

$$\gamma_i^{n+1} = \lambda_i \Delta\bar{\sigma} \bar{D}_i^{-1} + \beta_i \gamma_i^n \quad (\text{Eq. 4-9})$$

Note in this method, storage of all the previous data like γ_i , ε_i , σ from 1 to n-1 step is not necessary, which greatly reduce the computational cost.

4.2 CYCLIC CREEP

The cyclic creep of concrete, also known as fatigue creep, is the long-term behavior caused by the cyclic load. This load results in the fatigue growth of pre-existing microcracks in hydrated cement which leads to either an additional deformation (Bažant, 1968) to the static creep or an acceleration of the static creep (Bažant and Panula, 1979). Since it was experimentally detected in 1906, many investigation has been done to develop a generally accepted theory and constitutive law for the cyclic creep.

In this study, a micro-mechanical model for cyclic creep developed by Bažant and Hubler (2014) is used. In the model, three-dimensional planar microcrack of size a is considered. For tensile loading, mode I (crack opening mode) is concerned, and for

compression loading a combination of modes II (crack sliding mode) and III (tearing mode) is relevant. The growth of the crack is assumed to be in a self-similar way that expand in a certain scale. The energy release rate due to this growth can be expressed as (Bažant and Hubler, 2014):

$$G = \frac{\gamma_1}{a} \left[\frac{\partial \Pi^*}{\partial a} \right]_{\sigma} \quad (\text{Eq. 4-10})$$

where Π^* is the complementary energy per microcrack; σ is the applied remote stress; γ_1 is a dimensionless constant characterizing the geometry. Next the effective stress intensity factor based the average energy release rate can be expressed as (Bažant and Hubler, 2014):

$$K = \sqrt{GE} \quad (\text{Eq. 4-11})$$

where E is the Young's elastic modulus. For the sake of simplicity, mode I will be used here $K = K_I = 2\sigma\sqrt{a/\pi}$ (Tada et al., 1973). Therefore, Eq. 4-11 can be rewrite as (Bažant and Hubler, 2014):

$$G = \gamma_2 a \sigma^2 / E \quad (\text{Eq. 4-12})$$

where, γ_2 is a dimensionless shape factor $\gamma_2 = 4/\pi$. By substituting Eq. 4-12 in to Eq. 4-10 with integration, one gets:

$$\Pi^* = \frac{\gamma_2 \sigma^2}{3\gamma_1 E} a^3 \quad (\text{Eq. 4-13})$$

Suppose the volume per microcrack to be l_c^3 and all the microcracks to be perpendicular to the direction of applied stress. According to the Castigliano's theorem (Castigliano, 1873), the displacement u per crack can be calculated as:

$$u = \left[\frac{\partial \Pi^*}{\partial P} \right]_a = \frac{1}{l_c^2} \left[\frac{\partial \Pi^*}{\partial \sigma} \right]_a = \frac{\gamma_0}{El_c^2} \sigma a^3 \quad (\text{Eq. 4-14})$$

where P is the remote applied force that $P = l_c^2 \sigma$ and γ_0 is a dimensionless constant characterizing the geometry $\gamma_0 = 2\gamma_2 / 3\gamma_1$. Then the macroscopic strain can be calculated as (Bažant and Hubler, 2014):

$$\varepsilon^{cc} = \frac{u}{l_c} = \frac{\gamma_0}{El_c^3} \sigma a^3 \quad (\text{Eq. 4-15})$$

Suppose the total microcrack size increment over N cycles is $\Delta a_N = a_N - a_0$. Where a_N is the crack size after N cycles and a_0 is the size before cycles. $\Delta a_N / a_0 \ll 1$ is assumed here because the creep strain in service is always small (Bažant and Hubler, 2014). In this case $(1 + \frac{\Delta a_N}{a_0})^3 \approx 1 + 3(\frac{\Delta a_N}{a_0})$. Then the strain increment for cyclic creep can be obtained as

(Bažant and Hubler, 2014):

$$\Delta \varepsilon^{cc} = \frac{\gamma_0}{El_c^3} \bar{\sigma} (a_N^3 - a_0^3) \approx 3\gamma_0 \frac{\bar{\sigma}}{E} \left(\frac{a_0}{l_c}\right)^3 \frac{\Delta a_N}{a_0} \quad (\text{Eq. 4-16})$$

Next, Paris law (Paris and Erdogan, 1963) is applied because it can accurately approximate the intermediate range of fatigue crack growth, which is relevant for creep deflections of structures in the service renege. Stress amplitude of cyclic loading $\Delta \bar{\sigma} = \bar{\sigma}_{\max} - \bar{\sigma}_{\min}$ and of stress intensity factor $\Delta K = K_{\max} - K_{\min}$ is considered here. According to Paris law, very large amplitudes and very high $\bar{\sigma}_{\max}$ and K_{\max} are not concerned because they are more valuable for failure analysis instead of deformation analysis in service stress range. Base on this precondition, Paris law can be expressed as (Paris and Erdogan, 1963):

$$\frac{\Delta a_N}{N} = \lambda \left(\frac{\Delta K}{K_c} \right)^m \quad (\text{Eq. 4-17})$$

where K_c is the critical stress intensity factor. λ and m are empirical constants. The amplitude ΔK is proportional to the remote applied stress amplitude and can be calculated as $\Delta K = c\sqrt{a}\Delta\bar{\sigma}$ (c is a dimensionless geometry constant). Eq. 4-17 can be rewrite as (Paris and Erdogan, 1963):

$$a_N - a_0 = \lambda \left(\frac{c\sqrt{a}\Delta\sigma}{K_c} \right)^m N \quad (\text{Eq. 4-18})$$

By substituting Eq. 4-18 into Eq. 4-16 one can obtain the strain increment of cyclic creep (Bažant and Hubler, 2014):

$$\Delta\varepsilon^{cc} = C_1 \bar{\sigma} \left(\frac{\Delta\sigma}{f'_c} \right)^m N \quad (\text{Eq. 4-19})$$

where C_1 is expressed as (Bažant and Hubler, 2014):

$$C_1 = \frac{3\gamma_0}{E} \frac{\lambda}{a_0} \left(\frac{ca_0}{l_c} \right)^3 \left(\frac{f'_c \sqrt{a_0}}{K_c} \right)^m \quad (\text{Eq. 4-20})$$

f'_c here is the standard compression strength of concrete. It can be noted from Eq. 4-19 that cyclic creep strain tensor ε^{cc} is depend on both $\bar{\sigma}$ and N linearly. This perfectly matches the experiment measurement and simplifies the structural analysis. In this study, the exponent value m is assumed to be 4 and the coefficient C_1 is about 46×10^{-6} .

4.3 SHRINKAGE

The shrinkage is calculated based on the different recommendations. In this part, the ACI shrinkage model is utilized for illustration, the formulations of which are referred to the ACI

209.2R-08 (American Concrete Institute Committee, 2008). The shrinkage of concrete ε^{sh} at time t is calculated as:

$$\varepsilon^{sh}(t, t_c) = \frac{(t - t_c)^\alpha}{f + (t - t_c)^\alpha} \varepsilon_{shu} \quad \text{(Eq. 4-21)}$$

where t_c is the drying time. f and α are two shape and size constants to define the time-ratio part. According to ACI 209.2R-08 (American Concrete Institute Committee, 2008), for the standard condition, the average ultimate shrinkage strain ε_{shu} is suggest as $\varepsilon_{shu} = 780 \times 10^{-6}$ mm/mm .

5.0 NUMERICAL IMPLEMENTAION

5.1 GENERAL IMPLEMENTATION

In the implementation, all the variables at the beginning of current step, whose values are from the previous step, are marked as $(\cdot)^n$, and the updated values at the end of current step are marked as $(\cdot)^{n+1}$. The increment of the tensor is the difference between the updated value and the previous value such that $\Delta \varepsilon_{ij} = (\varepsilon_{ij})^{n+1} - (\varepsilon_{ij})^n$.

By taking the time derivative of Eq. 2-1, the total incremental strain tensor can be obtained:

$$\Delta \varepsilon_{ij} = \underbrace{(\Delta \varepsilon_{ij}^e + \Delta \varepsilon_{ij}^p)}_{\Delta \varepsilon_{ij}^i} + \underbrace{(\Delta \varepsilon_{ij}^{sc} + \Delta \varepsilon_{ij}^{cc} + \Delta \varepsilon_{ij}^{sh})}_{\Delta \varepsilon_{ij}^t} \quad (\text{Eq. 5-1})$$

Note that the total incremental strain tensor $\Delta \varepsilon_{ij}$ will be automatically given in ABAQUS.

The effective stress tensor $\bar{\sigma}_{ij}^{n+1}$ can be updated from $\bar{\sigma}_{ij}^n$ in the last time step:

$$\bar{\sigma}_{ij}^{n+1} = \bar{\sigma}_{ij}^n + \Delta \bar{\sigma}_{ij} \quad (\text{Eq. 5-2})$$

Then, the damaged stress tensor σ_{ij}^{n+1} can be transferred from the effective stress tensor $\bar{\sigma}_{ij}^{n+1}$ as:

$$\sigma_{ij}^{n+1} = (1 - \Phi^{n+1}) \bar{\sigma}_{ij}^{n+1} \quad (\text{Eq. 5-3})$$

Note that the increment of the effective stress $\Delta\bar{\sigma}_{ij}$ in a Kelvin unit equals that in the elastic spring. With the substitution of Eq. 5-1, the incremental effective stress $\Delta\bar{\sigma}_{ij}$ of the Kelvin chain unit and elastic spring can be written according to Hook's law as:

$$\Delta\bar{\sigma}_{ij} = \bar{E}_{ijkl}'' (\Delta\varepsilon_{kl}^e) = \bar{E}_{ijkl}'' (\Delta\varepsilon_{kl} - \Delta\varepsilon_{kl}^p - \Delta\varepsilon_{kl}^{sc} - \Delta\varepsilon_{kl}^{cc} - \Delta\varepsilon_{kl}^{sh}) \quad (\text{Eq. 5-4})$$

From Eq. 5-1, the incremental instantaneous strain tensor consists of elastic and plastic parts as:

$$\Delta\varepsilon_{ij}^i = \Delta\varepsilon_{ij}^e + \Delta\varepsilon_{ij}^p = \Delta\varepsilon_{ij}^{ep} \quad (\text{Eq. 5-5})$$

In addition, $\Delta\varepsilon_{ij}^i$ is the difference between the total incremental strain tensor and the incremental memory-dependent strain tensors as:

$$\Delta\varepsilon_{ij}^{ep} = \Delta\varepsilon_{ij} - \Delta\varepsilon_{ij}^{cc} - \Delta\varepsilon_{ij}^{sh} - \Delta\varepsilon_{ij}^{sc} \quad (\text{Eq. 5-6})$$

Note that the incremental static creep $\Delta\varepsilon^{sc}$ can be obtained from the previous time step by Eq. 4-8:

$$\Delta\varepsilon^{sc} = \sum_{i=1}^M \gamma_i^n (1 - e^{-\Delta t/\tau_i}) \quad (\text{Eq. 5-7})$$

The incremental cyclic creep $\Delta\varepsilon^{cc}$ can be obtained by Eq. 4-19 with the effective stress tensor from the last time step $\bar{\sigma}^n$:

$$\Delta\varepsilon^{cc} = C_1 \bar{\sigma}^n \left(\frac{\Delta\sigma^{cc}}{f_c'} \right)^m N \quad (\text{Eq. 5-8})$$

The incremental shrinkage $\Delta\varepsilon^{sh}$ (e.g. in ACI model) can be obtained by Eq. 4-21 as:

$$\Delta\varepsilon^{sh} = \left[\frac{(t_{n+1} - t_c)^\alpha}{f + (t_{n+1} - t_c)^\alpha} - \frac{(t_n - t_c)^\alpha}{f + (t_n - t_c)^\alpha} \right] \mathcal{E}_{shu} \quad (\text{Eq. 5-9})$$

The next job is to calculate the incremental elastic strain $\Delta\varepsilon_{ij}^e$ and the incremental plastic strain $\Delta\varepsilon_{ij}^p$, both of which are dependent on the effective stress tensor $\bar{\sigma}^{n+1}$ at current

time step. This calculation is realized by using the classical radial returning mapping algorithm (Simo and Huges, 1998) that:

$$\bar{\sigma}_{ij}^{n+1} = \bar{\sigma}_{ij}^n + \bar{E}_{ijkl}(\Delta \varepsilon_{kl}^{ep} - \Delta \varepsilon_{kl}^p) = \bar{\sigma}_{ij}^{trial} - \Delta \lambda_p \bar{E}_{ijkl} \frac{\partial F^P}{\partial \bar{\sigma}_{ij}} \quad (\text{Eq. 5-10})$$

where $\bar{\sigma}_{ij}^{trial} = (\bar{\sigma}_{ij}^n) + \bar{E}_{ijkl} \Delta \varepsilon_{kl}^{ep}$ is the trial stress tensor. According to the plasticity consistency conditions (Eq. 3-39), if the trail stress is within the yield surface $f(\bar{\sigma}^{trial}, (c^\pm)^n) < 0$, concrete response is elastic. In this situation, the variables are updated as:

$$\Delta \lambda_p = 0 \quad (\text{Eq. 5-11})$$

$$\bar{\sigma}_{ij}^{n+1} = \bar{\sigma}_{ij}^{trial} \quad (\text{Eq. 5-12})$$

$$(\varepsilon_{ij}^p)^{n+1} = (\varepsilon_{ij}^p)^n \quad (\text{Eq. 5-13})$$

$$(c^\pm)^{n+1} = (c^\pm)^n \quad (\text{Eq. 5-14})$$

However, if the stress is on the yield surface, the calculation of plastic multiplier $\Delta \lambda_p$ is necessary to update the $\bar{\sigma}_{ij}^{n+1}$, $(\varepsilon_{ij}^p)^{n+1}$ and $(c^\pm)^{n+1}$. This calculation will be described in the section 5.2.

For the damage part, the damage variable Φ^{n+1} is evaluated and used to transfer the effective stress tensor $\bar{\sigma}_{ij}^{n+1}$ to the real stress tensor σ_{ij}^{n+1} . This evolution will be described in the section 5.3.

5.2 CALCULATION OF THE PLASTIC MULTIPLIER

The goal in this part is to calculate the plastic multiplier $\Delta\lambda_p$ in order to update the $\bar{\sigma}_{ij}^{n+1}$, $(\varepsilon_{ij}^p)^{n+1}$ and $(c^\pm)^{n+1}$. According to the plasticity consistency conditions (Eq. 3-39), $\Delta\lambda_p$ needs to be calculated, when the stress at the end of current step is on the yield surface with loading condition. With the substitution of the yield function (Eq. 3-12), the following expression can be obtained:

$$f(\bar{\sigma}^{n+1}, (c^\pm)^{n+1}) = \sqrt{3J_2^{n+1}} + \alpha\bar{I}_1^{n+1} + \beta(\kappa^\pm)^{n+1} H(\hat{\sigma}_{\max}^{n+1}) \hat{\sigma}_{\max}^{n+1} - (1-\alpha)c^-(\kappa^-)^{n+1} = 0 \quad (\text{Eq. 5-15})$$

By substituting the consistent conditions (Eq. 3-39) into previous function, one can obtain:

$$f^{n+1} = f^n + \frac{\partial f}{\partial \bar{\sigma}_{ij}} \Delta\bar{\sigma}_{ij} + \frac{\partial f}{\partial \hat{\sigma}_{\max}} \Delta\hat{\sigma}_{\max} + \frac{\partial f}{\partial \kappa^+} \Delta\kappa^+ + \frac{\partial f}{\partial \kappa^-} \Delta\kappa^- = 0 \quad (\text{Eq. 5-16})$$

where $\Delta\bar{\sigma}_{ij}$ is expressed as (Taqieddin, 2008):

$$\Delta\bar{\sigma}_{ij} = \Delta\bar{\sigma}_{ij}^{trial} - \Delta\lambda_p [\sqrt{6}\bar{G} \frac{\bar{S}_{ij}^{trial}}{\sqrt{\bar{S}_{ij}^{trial}}} + 3\bar{K}a^p \delta_{ij}] \quad (\text{Eq. 5-17})$$

$\Delta\hat{\sigma}_{\max}$ is expressed as (Taqieddin, 2008):

$$\Delta\hat{\sigma}_{\max} = \Delta\hat{\sigma}_{\max}^{trial} - \Delta\lambda_p [\sqrt{6}\bar{G} \frac{\hat{\sigma}_{\max}^{trial}}{\sqrt{\bar{S}_{ij}^{trial}}} + (3\bar{K}a^p \delta_{ij} - \sqrt{\frac{2}{3}}\bar{G} \frac{I_1}{\sqrt{\bar{S}_{ij}^{trial}}})] \quad (\text{Eq. 5-18})$$

$\Delta\kappa^+$ is from Eq. 3-14 and Eq. 3-36:

$$\Delta\kappa^+ = r \cdot \Delta\lambda_p \frac{\partial F^p}{\partial \hat{\sigma}_{\max}} \quad (\text{Eq. 5-19})$$

$\Delta\kappa^-$ is from Eq. 3-15 and Eq. 3-36:

$$\Delta\kappa^- = -(1-r) \cdot (\Delta\lambda_p) \frac{\partial F^P}{\partial \hat{\sigma}_{\min}^-} \quad (\text{Eq. 5-20})$$

and therefore, by taking the $\Delta\bar{\sigma}_{ij}$, $\Delta\hat{\sigma}_{\max}^+$, $\Delta\kappa^+$ and $\Delta\kappa^-$ derivative of plastic yield surface f , the following expressions can be obtained:

$$\frac{\partial f}{\partial \bar{\sigma}_{ij}} = \sqrt{\frac{3}{2}} \frac{\bar{S}_{ij}^{trial}}{\|\hat{S}_{mn}^{trial}\|} + \alpha_p \delta_{ij} \quad (\text{Eq. 5-21})$$

$$\frac{\partial f}{\partial \hat{\sigma}_{\max}^+} = \sqrt{\frac{3}{2}} \frac{(\hat{\sigma}_{ij}^{trial} - \frac{1}{3} \bar{I}_1^{trial})}{\|\hat{S}_{mn}^{trial}\|} + \alpha_p = \beta(\kappa^\pm)^{n+1} H(\hat{\sigma}_{\max}^{n+1}) \quad (\text{Eq. 5-22})$$

$$\frac{\partial f}{\partial \kappa^+} = -\frac{(1-\alpha)c^-h}{(c^+)^2} \langle \hat{\sigma}_{\max}^{n+1} \rangle \quad (\text{Eq. 5-23})$$

$$\frac{\partial f}{\partial \kappa^-} = (1-\alpha)Q\omega \exp(-\omega\kappa^-) \left[\frac{\langle \hat{\sigma}_{\max}^{n+1} \rangle}{c^+} - 1 \right] \quad (\text{Eq. 5-24})$$

Finally, by substituting Eq. 5-21, Eq. 5-22, Eq. 5-23 and Eq. 5-24 into Eq. 5-16, the plastic multiplier $\Delta\lambda_p$ can be expressed as (Taqieddin, 2008):

$$\Delta\lambda_p = \frac{f^{trial}}{H} \quad (\text{Eq. 5-25})$$

where f^{trial} in the above equation is expressed as:

$$f^{trial} = f^n + \frac{\partial f}{\partial \bar{\sigma}_{ij}} \Delta\bar{\sigma}_{ij}^{trial} + \frac{\partial f}{\partial \hat{\sigma}_{\max}^+} \Delta\hat{\sigma}_{ij}^{trial} \quad (\text{Eq. 5-26})$$

and H is expressed as:

$$H = \frac{\partial f}{\partial \bar{\sigma}_{ij}} \left[\sqrt{6G} \frac{\bar{S}_{ij}^{trial}}{\sqrt{\bar{S}_{ij}^{trial}}} + 3\bar{K}a^p \delta_{ij} \right] + \frac{\partial f}{\partial \hat{\sigma}_{\max}^+} \left[\sqrt{6G} \frac{\hat{\sigma}_{\max}^+}{\sqrt{\bar{S}_{ij}^{trial}}} \right. \\ \left. + (3\bar{K}a^p \delta_{ij} - \sqrt{\frac{2}{3}} \bar{G} \frac{I_1}{\sqrt{\bar{S}_{ij}^{trial}}}) \right] - r \frac{\partial f}{\partial \kappa^+} \frac{\partial F^P}{\partial \hat{\sigma}_{\max}^+} + (1-r) \frac{\partial f}{\partial \kappa^-} (\Delta\lambda_p) \frac{\partial F^P}{\partial \hat{\sigma}_{\min}^-} \quad (\text{Eq. 5-27})$$

$\frac{\partial F^P}{\partial \hat{\sigma}_{\max,\min}^\pm}$ in the Eq. 5-27 is calculated as (Taqieddin, 2008):

$$\frac{\partial F^p}{\partial \hat{\sigma}_{\max, \min}} = \sqrt{\frac{3}{2}} \frac{\left(\hat{\sigma}_{\max, \min}^{trial} - \frac{1}{3} \bar{I}_1^{trial} \right)}{\left\| \hat{S}_{mn}^{trial} \right\|} + \alpha_p \quad (\text{Eq. 5-28})$$

5.3 EVOLUTION OF THE DAMAGE VARIABLES

The damage variable Φ^{n+1} at the $n+1$ step is calculated here which is related to the effective stress tensor $\bar{\sigma}_{ij}^{n+1}$ and the elastic strain tensor $(\varepsilon_{ij}^e)^{n+1}$ by the end of current step. Whether the Φ^{n+1} need to be updated from the last step is depend on the damage consistency conditions (Eq. 3-42). The damage surface from Eq. 3-40 can be rewritten with step indication as:

$$g^\pm = (Y^\pm)^{n+1} - Y_0^\pm - (Z^\pm)^n \leq 0 \quad (\text{Eq. 5-29})$$

The damage thermodynamic forces here are calculated as (Eq. 3-31):

$$Y^\pm - \frac{1}{2} \frac{\left\| (\bar{\sigma}_{ij}^\pm)^{n+1} \right\|}{\left\| (\bar{\sigma}_{ij}^\pm)^{n+1} \right\|} \left\{ (\varepsilon_{ij}^e)^{n+1} \bar{E}_{ijkl} (\varepsilon_{kl}^e)^{n+1} - \frac{1}{9} \left[\frac{1}{1 + cY^\pm \exp(-d \cdot Y^\pm)} \right] ((\varepsilon_{ij}^e)^{n+1})^2 \delta_{ij} \bar{E}_{ijkl} \delta_{kl} \right\} = 0 \quad (\text{Eq. 5-30})$$

The tensile and compressive effective stress tensors $\bar{\sigma}_{ij}^\pm$ can be derived by spectral decomposition introduced from Eq. 3-8 to Eq. 3-10. Note that Eq. 5-30 is a nonlinear function of the damage thermodynamic forces Y^\pm , which can be written as $K(Y^\pm) = 0$ for simplicity, and the Newton-Raphson iterative method is utilized to solve it such that (Taqieddin, 2008):

$$Y_{m+1}^\pm = Y_m^\pm + \Delta Y^\pm = Y_m^\pm - K(Y_m^\pm) / \left(\frac{\partial K(Y^\pm)}{\partial Y^\pm} \right) \quad (\text{Eq. 5-31})$$

With

$$\frac{\partial K(Y^\pm)}{\partial Y^\pm} = 1 - \frac{1}{2} \frac{\|(\bar{\sigma}_{ij}^\pm)^{n+1}\|}{\|(\bar{\sigma}_{ij}^\pm)^{n+1}\|} \left\{ \frac{1}{9} \left[\frac{c \exp(-d \cdot Y^\pm) - cdY^\pm \cdot \exp(-d \cdot Y^\pm)}{(1 + cY^\pm \exp(-d \cdot Y^\pm))^2} \right] ((\varepsilon_{ij}^e)^{n+1})^2 \delta_{ij} \bar{E}_{ijkl} \delta_{kl} \right\} \quad (\text{Eq. 5-32})$$

Because the result of this iterative procedure is highly depend on the initially guess, here the first guess Y_0^\pm is suggested as (Taqieddin, 2008):

$$Y_0^\pm = \frac{1}{2} \frac{\|(\bar{\sigma}_{ij}^\pm)^{n+1}\|}{\|(\bar{\sigma}_{ij}^\pm)^{n+1}\|} ((\varepsilon_{ij}^e)^{n+1} \bar{E}_{ijkl} (\varepsilon_{kl}^e)^{n+1}) \quad (\text{Eq. 5-33})$$

When converge to a tolerance criterion, this iterative procedure will stop, and outcome is regard as the damage thermodynamic forces $(Y^\pm)^{n+1}$ at the n+1 step.

$(Z^\pm)^n$ in Eq. 5-29 is the softening parameters from the previous step.

By substituting $(Y^\pm)^{n+1}$, Y_0^\pm and $(Z^\pm)^n$ in to the Eq. 5-29, damage surface g^\pm can be obtained. According to the damage consistency conditions (Eq. 3-42), if the $g^+ < 0$ and $g^- < 0$, the damage variable needs not to be updated ($(\Phi^\pm)^{n+1} = (\Phi^\pm)^n$, $(\Phi)^{n+1} = (\Phi)^n$), and real stress tensor σ_{ij}^{n+1} equals the updated effective stress tensor $\bar{\sigma}_{ij}^{n+1}$, and if $g^\pm = 0$ and $\dot{g}^\pm > 0$, the damage evolves, and the tensile/compressive damage variables are updated as (Tao and Philips, 2005 and Taqieddin, 2008):

$$(\Phi^\pm)^{n+1} = 1 - \frac{1}{1 + (a^\pm [(Y^\pm)^{n+1} - Y_0^\pm])^{b^\pm}} \quad (\text{Eq. 5-34})$$

Then the total damage variable can be calculated by Eq. 3-11 as (Tao and Philips, 2005):

$$\Phi^{n+1} = \frac{\|(\sigma_{ij}^+)^{n+1}\| (\Phi^+)^{n+1} + \|(\sigma_{ij}^-)^{n+1}\| (\Phi^-)^{n+1}}{\|(\sigma_{ij}^\pm)^{n+1}\|} \quad (\text{Eq. 5-35})$$

Meanwhile, the softening parameters should be updated as (Taqieddin, 2008):

$$(Z^\pm)^{n+1} = \frac{1}{a^\pm} \left(\frac{(\Phi^\pm)^{n+1}}{1 - (\Phi^\pm)^{n+1}} \right)^{\frac{1}{b^\pm}} \quad (\text{Eq. 5-36})$$

5.4 OVERALL FLOWCHART

The overall flowchart of the numerical implementation based on the unified model in ABAQUS is shown from Figure 3 to Figure 5.

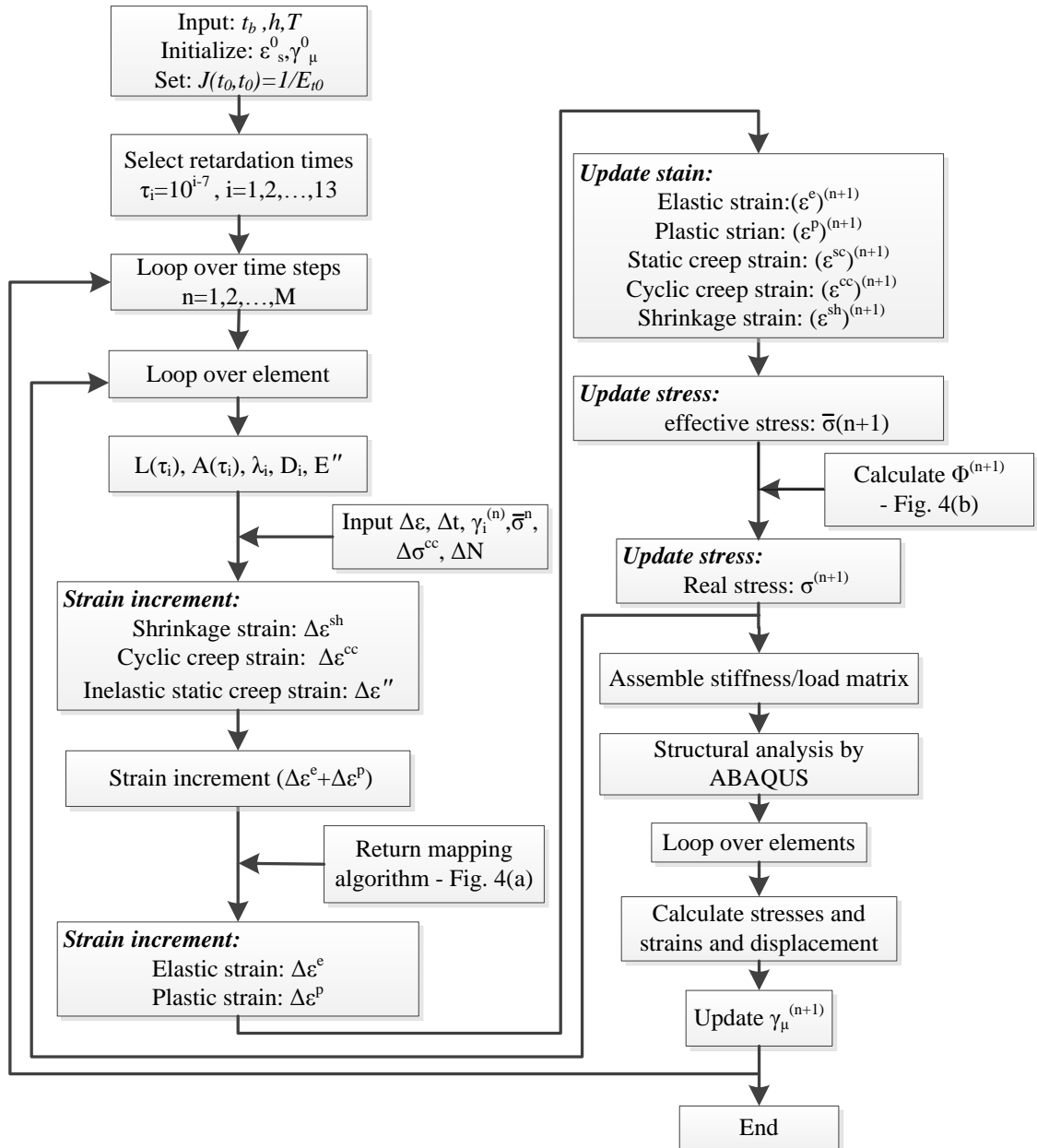


Figure 3. The overall flowchart of the numerical implementation based on the unified model by

ABAQUS

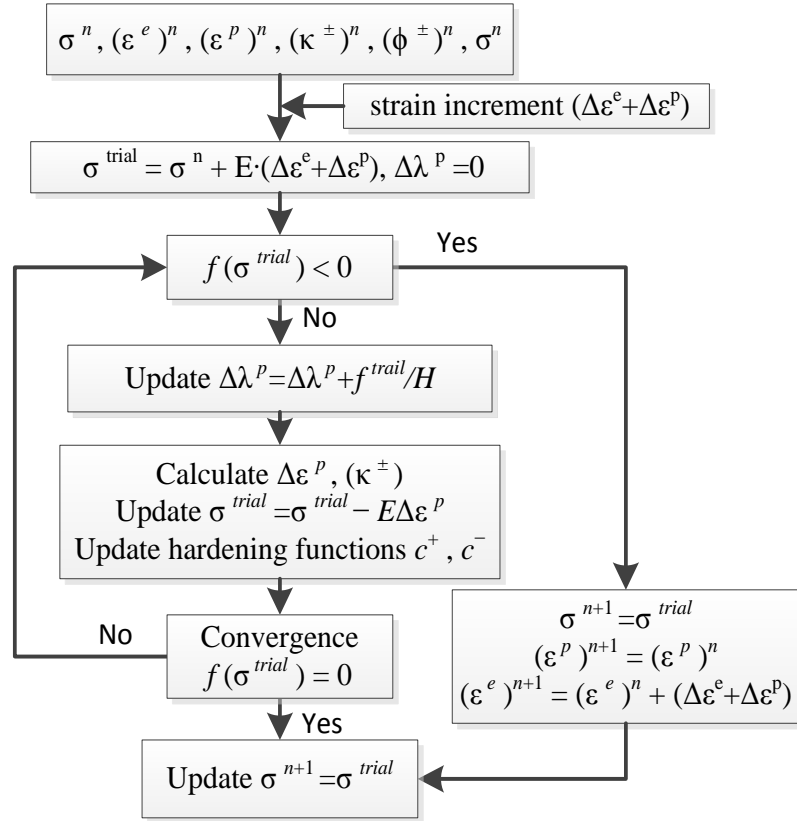


Figure 4. The flowchart of return mapping algorithm

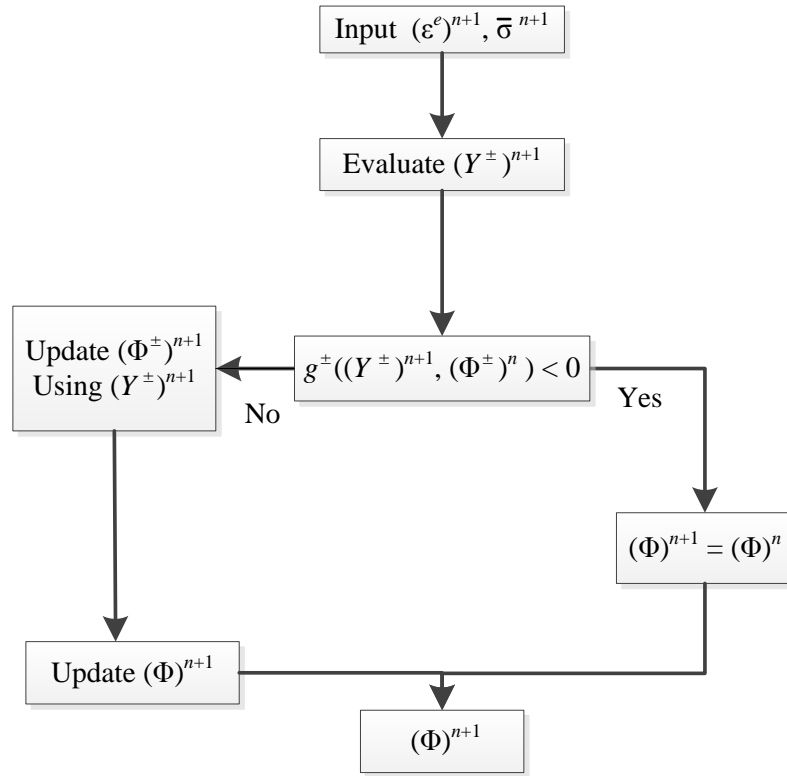


Figure 5. The flowchart of damage variable calculation

6.0 CASE STUDY

To verify the effectiveness of the unified concrete model in predicting the long-term performance of large-span prestressed concrete bridge with heavy traffic load, Humen Bridge, as a suitable choice, is selected and studied here. The necessary details are described and the finite element model along with the simulation approach is introduced. Then, the simulation results based on the pure viscoelastic analysis and the unified model are derived and compared with the real measurements. Finally, the results are analyzed and the accuracy of the unified concrete model is evaluate.

6.1 BRIDGE INTRODUCTION

Humen Bridge is a three-span (150 m+ 270 m +150 m) cast-in-situ rigid frame segmentally prestressed concrete bridge located at Pearl River Delta in Guangdong Province, China. Its 270 m main span overtakes the main span of Gateway Bridge in Australia (260 m) and became the longest span for the same type prestressed concrete bridge in the world when it was in operation in June, 1997. The bridge consists of two identical single box girder spans.

Carrying the opposite traffic flow, these two spans are independent with each other. The view of Humen Bridge is shown in Figure 6.

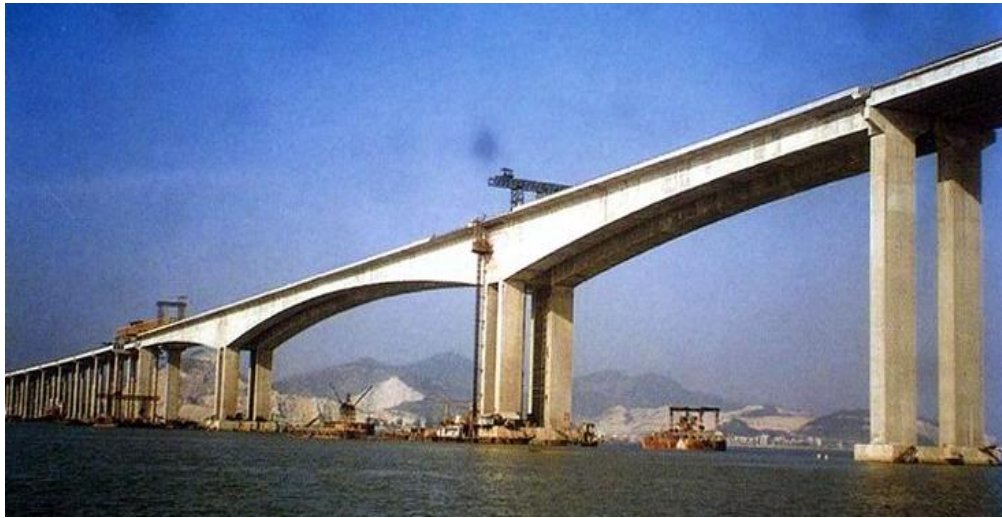


Figure 6. Humen Bridge Auxiliary Channel Bridge

6.1.1 Specific dimension

The span in Humen Bridge consists of a single box girder. The top length of the box girder is 15 m and the bottom length is 7 m. The height of the box girder is from 14.8 m at the pier to 5 m at the mid-span. The top slab has the consistent thickness along the traffic direction but it increases from 0.15 m at the exterior of the suspended top slab to 0.45 m at the intersection of the web and then decrease to 0.25 m at the middle of the cross-section. This change follows a linear format. The thickness of bottom slab varies from 1.3 m at pier to 0.32 m at mid-span and thickness of web is reduced from 0.8 m at the pier to 0.4 m at the mid-span. These two changes follow a quadratic parabolic curve. The specific dimension of the box girder is shown in Figure 7 and Figure 8.

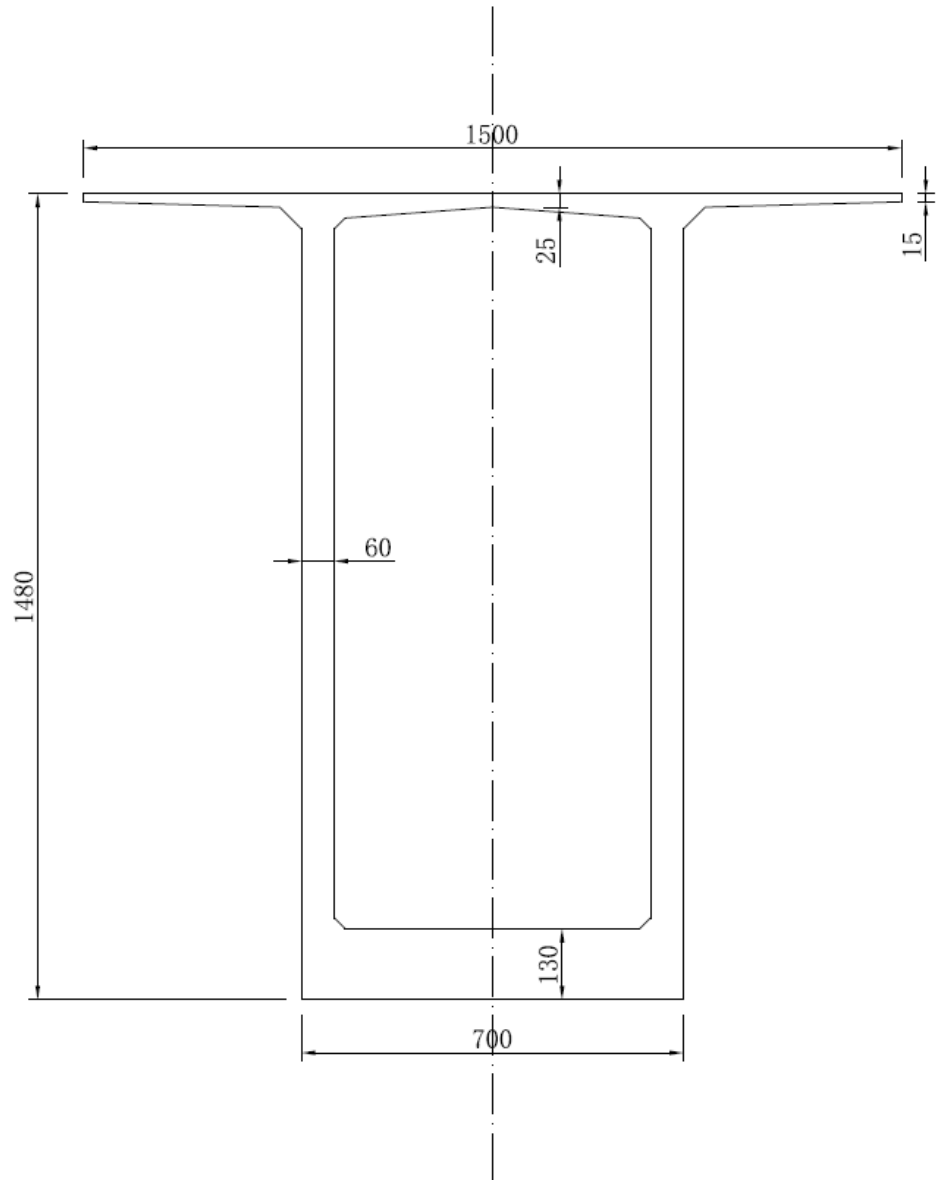


Figure 7. The dimension of cross-section at the pier (mm)

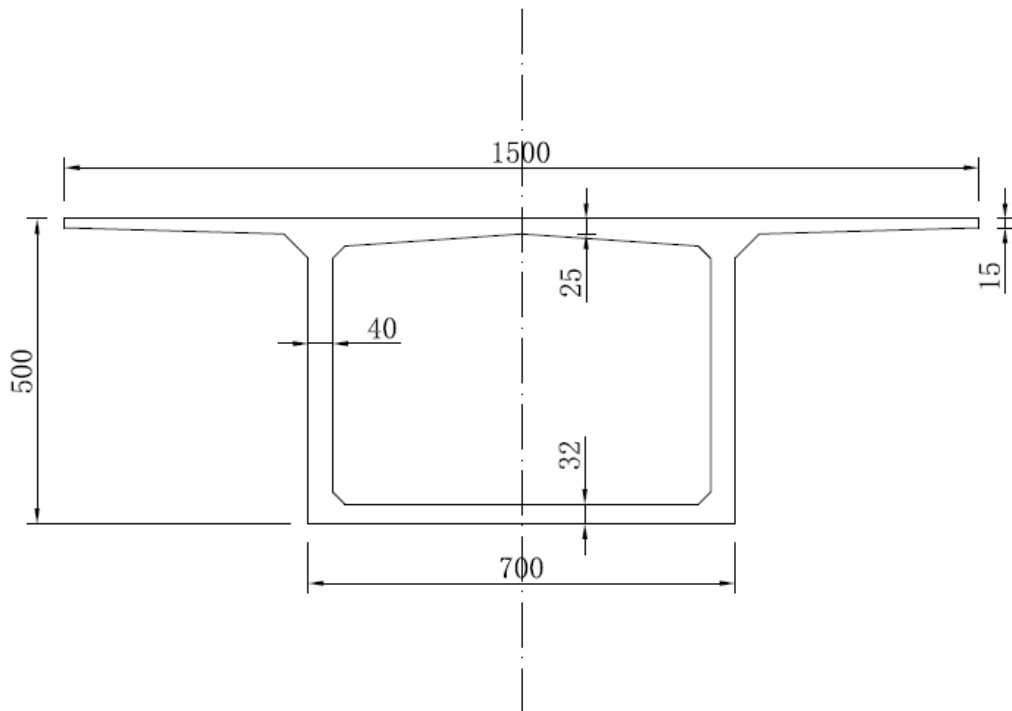


Figure 8. The dimension of cross-section at the middle span (mm)

6.1.2 Traffic investigation

Pearl River Delta in Guangdong province is one of the most industrialized and richest areas in China, where is close to the metropolitan, Hongkong. Because of this particular location, Humen Bridge has to carry the traffic flow inside Guangdong Province and flow between Guangdong Province and Hong Kong, which makes it carrying one of the largest traffic volume in the world.

With the assist of Highway toll system of Humen Bridge, the amount of the vehicles passing the bridge and the magnitude of their weight are recorded. According to the inspection report (Humen Bridge Auxiliary Bridge inspection report, 2011), the traffic volume increased from 6,381,541 in 1998 to 24,484,336 in 2010 (shown in Figure 9). This

large traffic volume may suggest that the cyclic creep and damage may be critical to the long-term deflection.

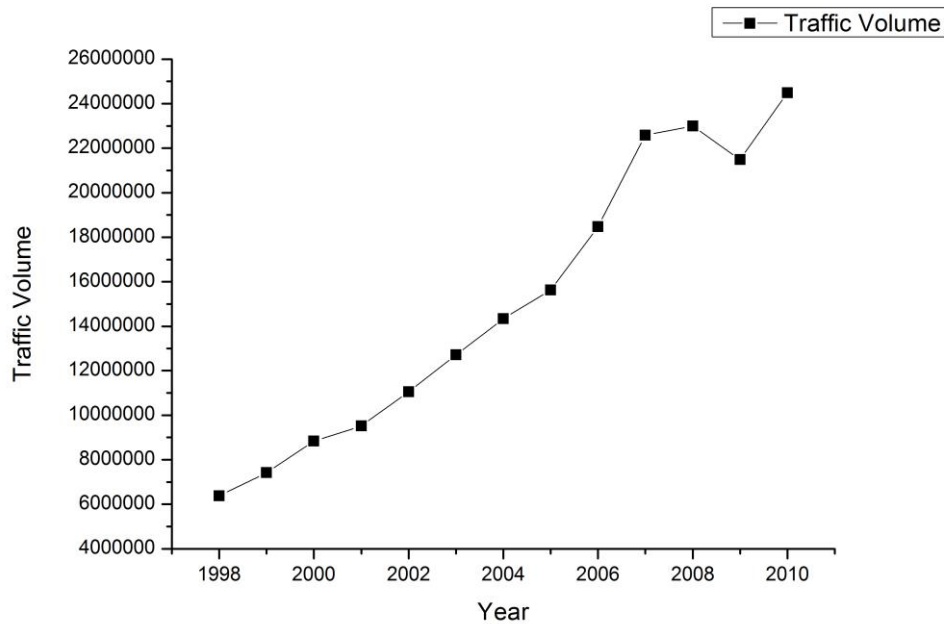


Figure 9. Traffic volume from 1998 to 2010

All the vehicles are classified into six types (Humen Bridge Auxiliary Bridge inspection report, 2011): type 1 represents for motorcycles whose weights are negligible and therefore it is not considered in the simulation; the type 2-6 stand for the different vehicles and are characterized by the increasing weight. The report also provides the specific proportion of these six types for each year and proportions from 1998 to 2002 are illustrated from Figure 10 to Figure 14. With the increase of total traffic volume, the amount of type 6 increased from 196,872 in 1998 to 460,140 in 2002, which grows about 234%. The exact volume of type 6 vehicles is shown in figure 15.

Table 1. Vehicle classification

	Type 1	Type 2	Type 3	Type 4	Type 5	Type 6
Weight (ton)	-	0-2	2-5	5-8	8-20	>20

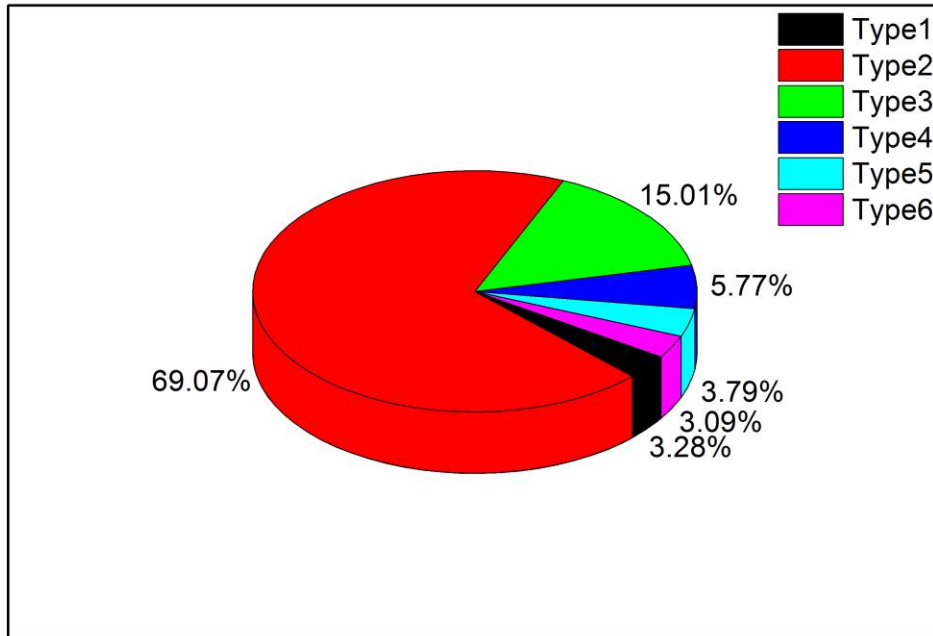


Figure 10. The volume proportion of the six types in 1998

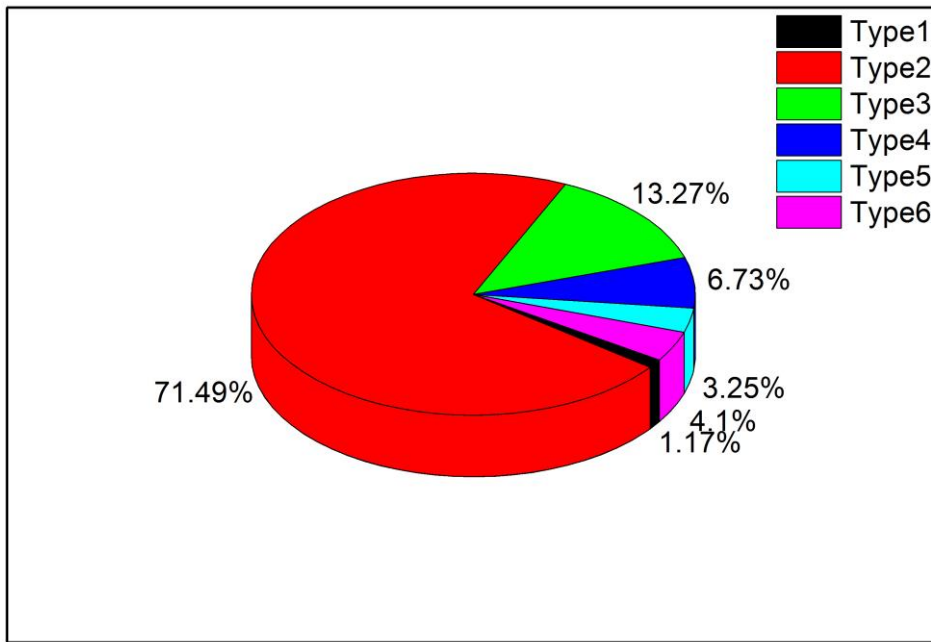


Figure 11. The volume proportion of the six types in 1999

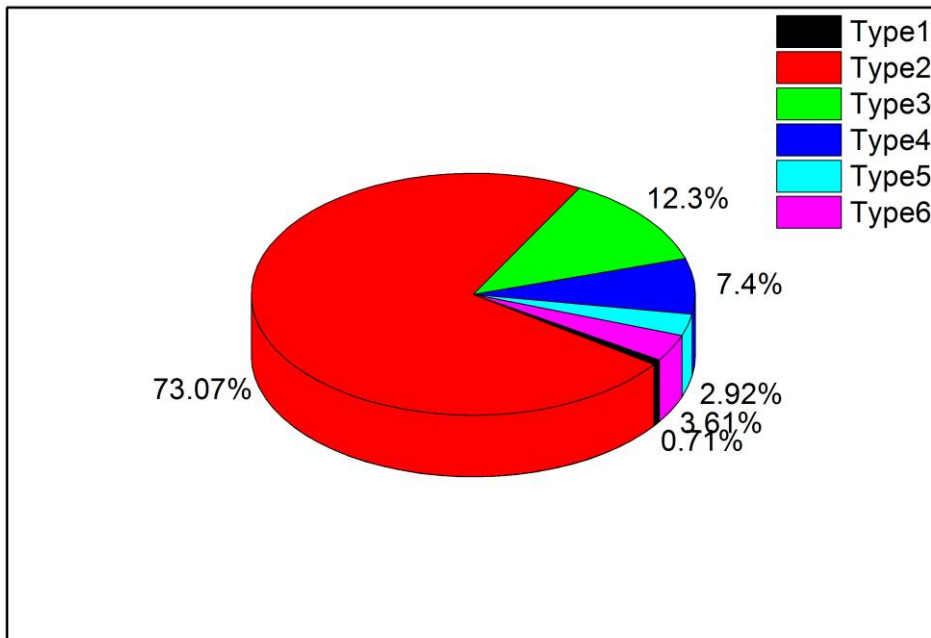


Figure 12. The volume proportion of the six types in 2000

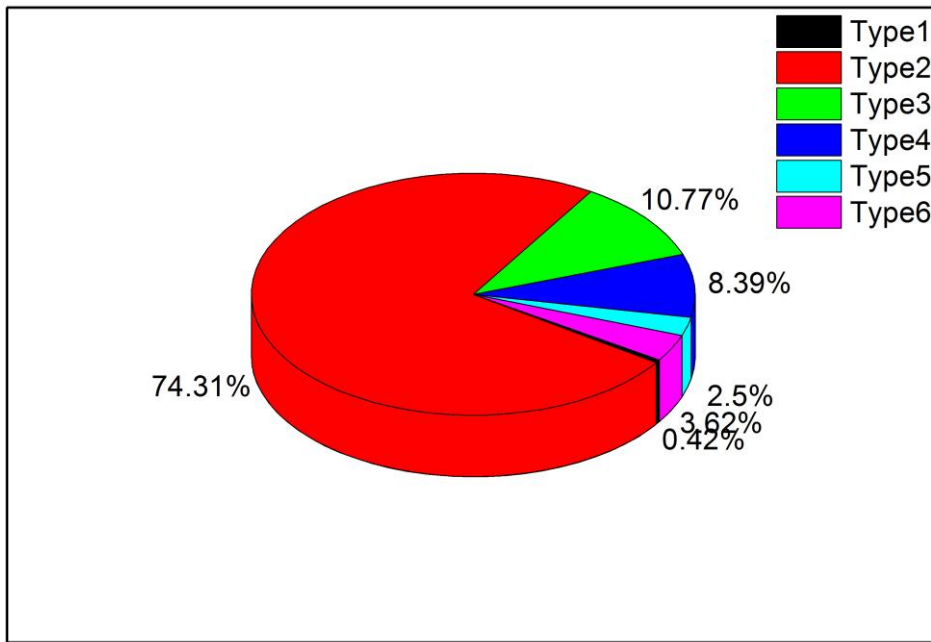


Figure 13. The volume proportion of the six types in 2001

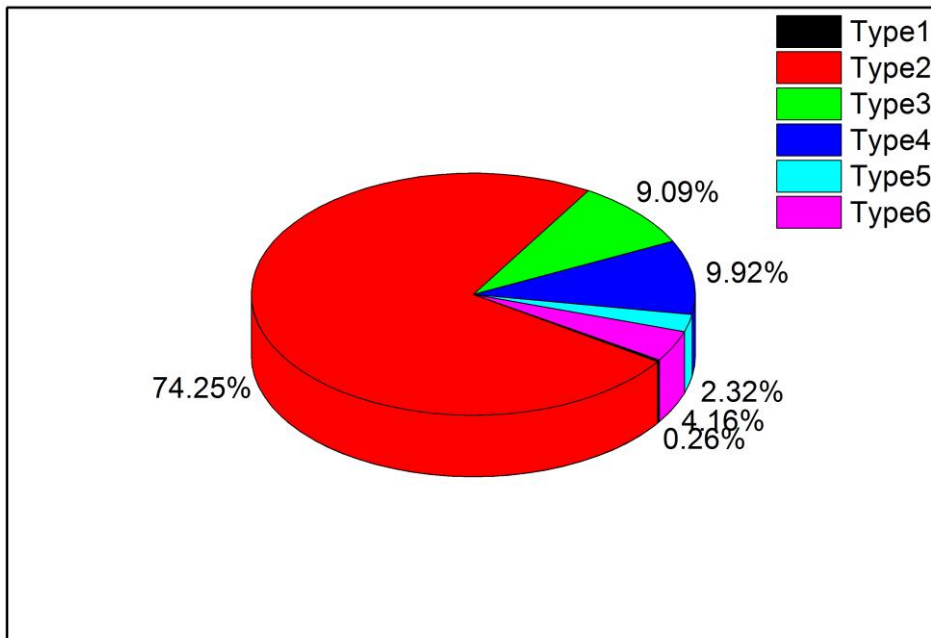


Figure 14. The volume proportion of the six types in 2002

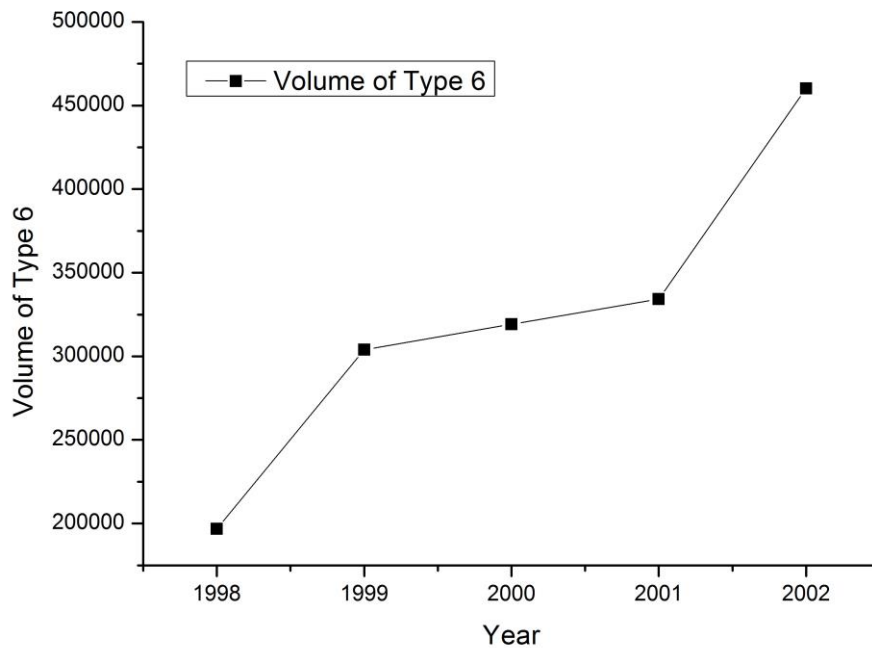


Figure 15. The volume of type 6 vehicles from 1998 to 2002

6.2 FINITE ELEMENT MODEL

The advanced 3D finite element modelling software ABAQUS is selected to simulate the long-term behavior of Humen Bridge. An advantage of this software is its user-subroutine UMAT providing a convenient way for users to define their own material properties, which perfectly meet the demand in this study. With the assistance of the blueprint, this bridge model is built in ABAQUS (Figure 16). Because of its symmetry both in longitudinal and transversal directions, half span and half cross-section of the span is simulated.

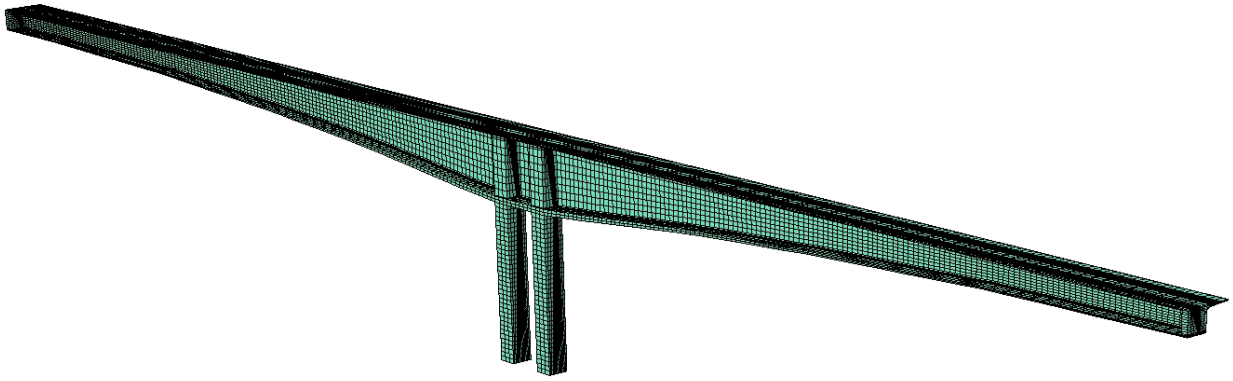


Figure 16. ABAQUS model for the Humen Bridge

In this study, concrete is modeled by 3D hexahedral isoparametric elements (C3D8 in ABAQUS) and prestressing tendons are modeled by 3D truss elements (T3D2 in ABAQUS). After meshing, 35,433 hexahedral elements and 23,222 truss elements are generated in the model. Because the influence of normal reinforcing tendons on the behaviors of prestressed concrete bridge is negligible, these rebars are not considered in this simulation. All the web and top/bottom slabs are meshed into two layers of C3D8 elements and the prestressing tendons are placed at the middle of them. Perfect bond is assumed between concrete and the prestressing tendons by sharing the same element nodes in this simulation. Trying to capture balanced cantilever construction procedure which leads to a complicated loading history both in the concrete and tendons, all the elements are deactivated at first and then progressively activated based on the construction sequence. The camber generated during construction is neglected in the deflection comparison to focus on the post-construction behavior.

In this model, 94 longitudinal prestressing tendons (ASTM A416-87A170) are applied to prestress the 69 segments. Among these tendons, 66 are cantilever tendons placed

inside the top slab and 28 are continuous tendons in the bottom slab. Besides the longitudinal tendons, the vertical prestressing tendons (32-mm diameter screw-thread steel) are placed in the web with 1 m spacing to increase the shear-resistant ability of the concrete girder. The detailed distribution of these tendons is illustrated in Figure 17. For each group of tendons, the prestress is applied 7 days after their anchoring segments casted. The initial prestressing level for longitudinal prestressing tendons is selected as 1080MPa and for the vertical prestressing tendons is about 400 MPa.

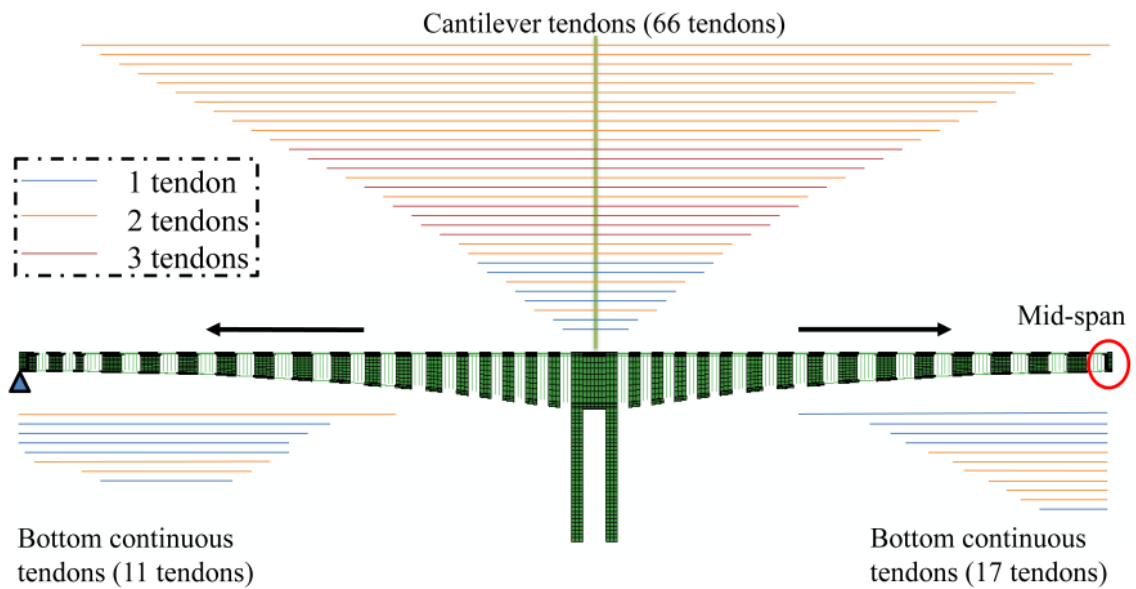


Figure 17. The detailed distribution of prestressing tendons

6.3 SIMULATION APPROACH

In this study, the Humen Bridge is simulated based on both pure viscoelastic analysis and the unified model. The pure viscoelastic analysis is based on ACI, fib MC2000 and B4 model,

separately. The ACI model is basically empirical where the only intrinsic parameter employed to represent concrete composition in its compliance formulas is the concrete strength f'_c . B4 model is adapted from the B3 model, whose creep is divided into basic creep and drying creep based on the solidification theory (Bažant and Prasannan 1989 a,b, Bažant and Baweja 2000). The basic creep is unbounded and consists of short-term strain, viscous strain and a flow term while the drying creep is bounded and related to moisture loss. As a new version, the fib MC2010 model is updated from the CEB-fib MC190 model also by splitting creep into basic creep and drying creep like B4 model. The unified concrete model will be implemented with the ACI, fib MC2000 and B4 model as its viscoelastic analysis respectively.

All intrinsic and extrinsic parameters are the same to emphasize the difference resulting from the compliance function. All the parameters are set as follows:

1. Design compressive strength $f'_c = 46$ MPa
2. Cement content $c = 523.5$ kg/m³
3. Water to cement ratio by weight $w/c = 0.35$
4. Aggregate to cement ratio by weight $a/c = 3.5$
5. Humidity h (70%)
6. Temperature T (20°C)
7. For the prestressing tendon: $E = 200$ GPa and $f_y = 1674$ MPa

All the implementations are realized by the user-subroutine UMAT in the ABAQUS.

In this simulation, the pure viscoelastic analysis based on three creep and shrinkage models without considering damage, plasticity and the cyclic creep are implemented respectively first. The results will be compared with each other and with the real measurements. Then the unified model with viscoelastic analyses based on three different models, considering damage, plasticity and the cyclic creep, are used to simulate the long-term behaviors. The outcome comparison is similar to the comparison of the pure viscoelastic analysis. Finally, the analysis and the conclusion can be drawn based on these comparisons.

6.4 SIMULATION RESULTS

6.4.1 The pure viscoelastic analysis

The deflections calculated based on pure viscoelastic analyses are analyzed here as a comparison with the deflections from unified model. The asymptote of long-term vertical deflection is directly governed by the compliance function because the concrete shrinkage and steel relaxation will die out with the increase of time. In this simulation, the vertical deformations at the middle point of the Bridge based on ACI, fib MC2010 and B4 models are calculated and plotted with 100 years both in the linear time scale (Figure 18) and logarithmic time scale (Figure 19). Note that the log time figure is plot here because the deflection tendency is more obvious when the compliance function is govern by a logarithmic term.

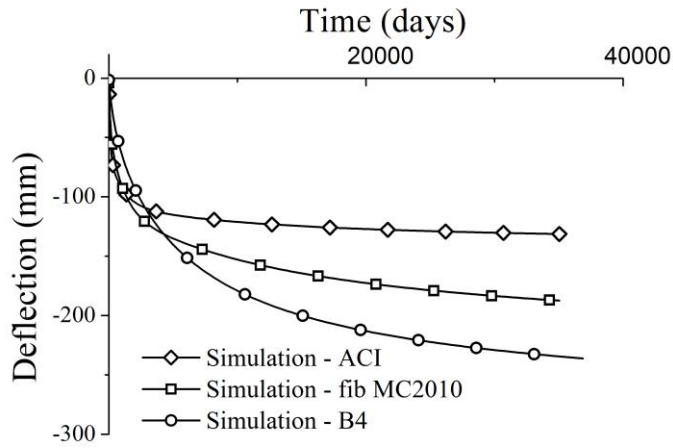


Figure 18. The deflection at the middle point for pure viscoelastic analysis with linear time scale

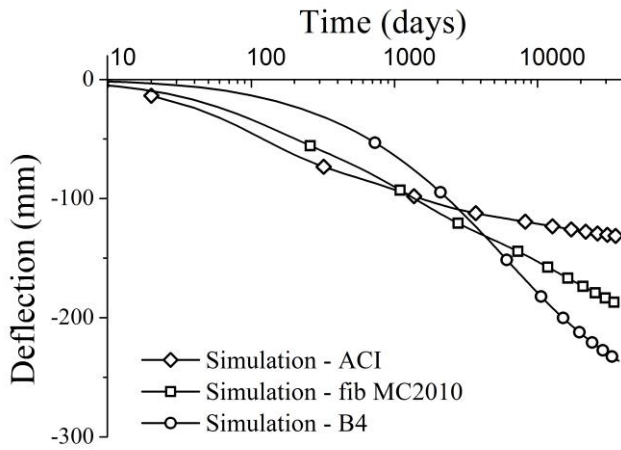


Figure 19. The deflection at the middle point for pure viscoelastic analysis with log time scale

The deflections here are calculated from the end of construction, which means no camber during construction is considered. From the Figure 18, and Figure 19, the values based on ACI, fib MC2010 and B4 are different from each other even with the same intrinsic and extrinsic parameters. Among these three deflections, the one based on ACI model is the

most conservative one. For this model, the compliance function is bounded which means creep will terminate after a certain time. According to the ACI formulas, this creep termination usually takes about 30 years and then the deflection curve will tend to a horizontal line. This can be shown in the Figure 18 that at about 30 years (10, 950 days), the deflection increases to about 120 mm and then stabilized. For the fib MC2010 and B4 model, the compliance functions consist of the bounded drying creep and logarithmic basic creep, which makes the functions unbounded. Governed by the logarithmic part in compliance functions, the decreasing tendencies of deflection evolution based on these two models are shown especially in Figure 19 with log time scale. However, although the deflection tendencies for fib MC2010 and B4 model are similar, the value for B4 model is greater than the fib MC2010 model after 3 years and this difference is increasing with time. By the time of 100 years, the deflection from B4 model develops to about 250 mm while the one from fib MC2010 model only reaches about 160 mm.

Next, the deflections based on pure viscoelastic analyses are compared with the in-situ measurements from the inspection report (Humen Bridge Auxiliary Bridge inspection report, 2011). In this report, the deflections of left span and right span are recorded from the completion of the bridge to 7 years, which is plotted in Figure 20 and Figure 21 along with the deflections based on ACI, fib MC2010 and B4 models. It is obvious that all the predicted deflections based on pure viscoelastic analyses are much smaller than the in-situ measurements. After 7 years, the vertical deflection prediction of ACI, fib MC2010 and B4

models are about 100 mm, 110 mm and 140 mm respectively while the measured value for left span and right span are about 210 mm and 220 mm respectively.

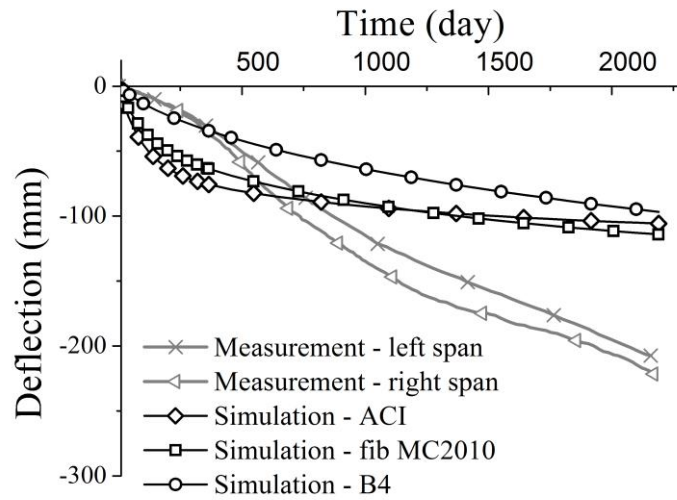


Figure 20. The comparison of deflections at middle point from measurements and simulations based on pure viscoelastic analysis models in 7 years with linear time scale

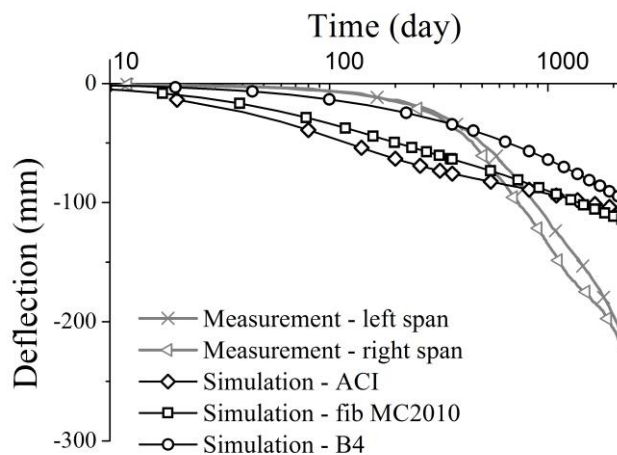


Figure 21. The comparison of deflections at middle point from measurements and simulations based on pure viscoelastic analysis models in 7 years with log time scale

The striking difference of deflection between the simulation value and real measurement suggests that the pure viscoelastic analysis based on the creep and shrinkage models, like ACI, fib MC2010 and B4 model, is insufficient in accurately predicting the vertical deflection for the large-span prestressed concrete bridge with heavy traffic like Humen Bridge. This is mainly because viscoelastic analysis ignores many phenomena and therefore, a more comprehensive model that can take all important factors into account is needed to improve the accuracy of prediction.

6.4.2 The unified model

In this section, the prediction of middle point deflection is demonstrated based on the unified model where the plasticity, damage, cyclic creep and other factors are considered. The creep and shrinkage models, ACI, fib MC2010 and B4 model, with the same intrinsic and extrinsic parameters are selected for the viscoelastic analysis in the unified concrete model. The results from the simulation are illustrated in Figure 22 and Figure 23, along with the real measurements both in linear time scale and log time scale.

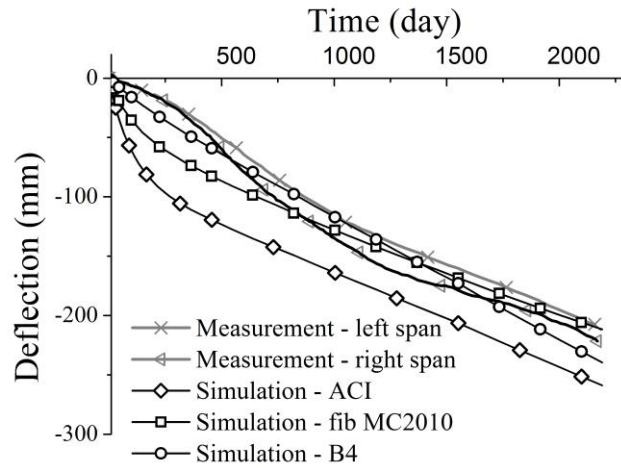


Figure 22. The comparison of deflections at middle point based on measurements and simulations

from the unified models in 7 years with linear time scale

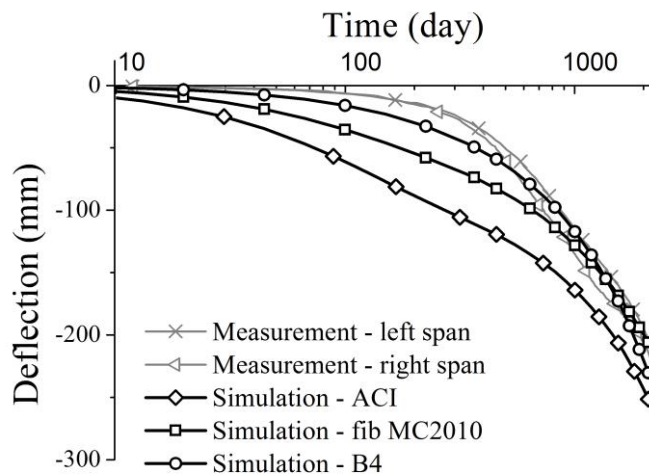


Figure 23. The comparison of deflections at middle point based on measurements and simulations

from the unified models in 7 years with log time scale

From Figure 22 and Figure 23, one can find that the simulations based on the unified concrete model match the real deflections quite well. After 7 years, the prediction based on

the unified model with ACI, fib MC2010 and B4 model is 258 mm, 212 mm, and 198 mm respectively while the measured value for left span and right span are about 210 mm, and 220 mm respectively. The simulation given by unified model with B4 model is almost as accurate as the fib MC2010 model after 3 years, however the results from B4 model is much more accurate than the other two simulations before 3 years. Therefore, considering the whole of 7 years, the unified concrete model with B4 creep and shrinkage model is the most effective material model.

In the inspection report (Humen Bridge Auxiliary Bridge inspection report, 2011), not only the deflection of middle point of the bridge, but also the deflection profiles are recorded from 1998 to 2002. Because the prediction at middle point from unified model with B4 creep and shrinkage model matches the measurements most well, the simulation results for deflection profiles based on this model are compared with the real deflections. The comparisons from the first year to the fifth year are illustrated from Figure 24 to Figure 28. The accuracy of these results is acceptable.

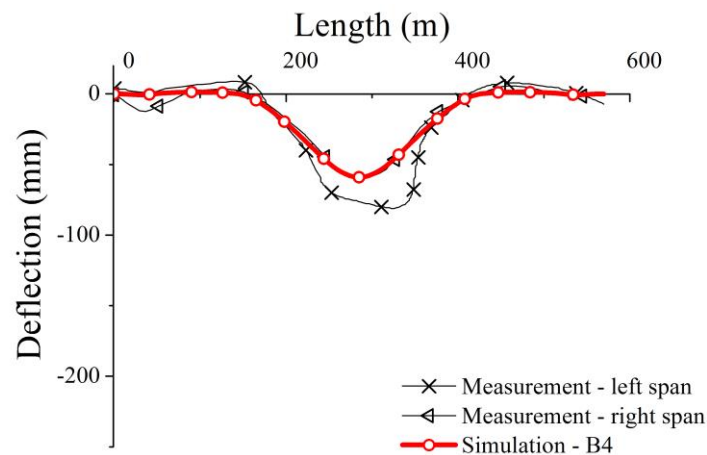


Figure 24. The first year profile from the unified model with B4 model and real measurements

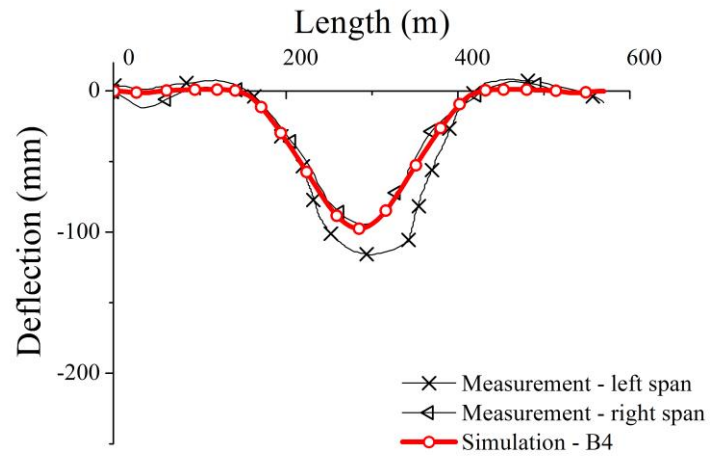


Figure 25. The second year profile from the unified model with B4 model and real measurements

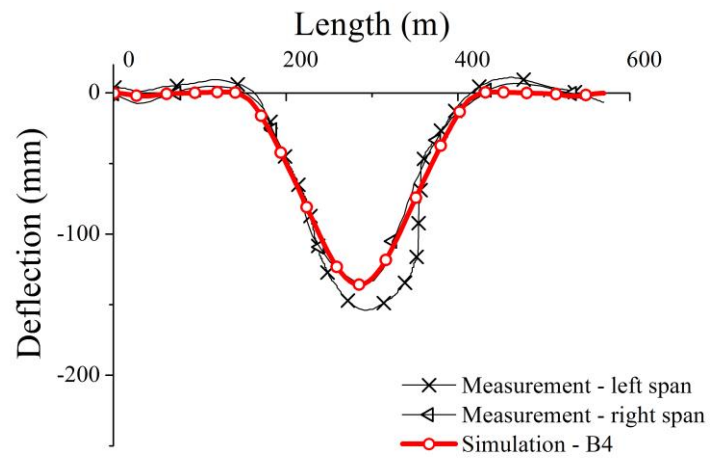


Figure 26. The third year profile from the unified model with B4 model and real measurements

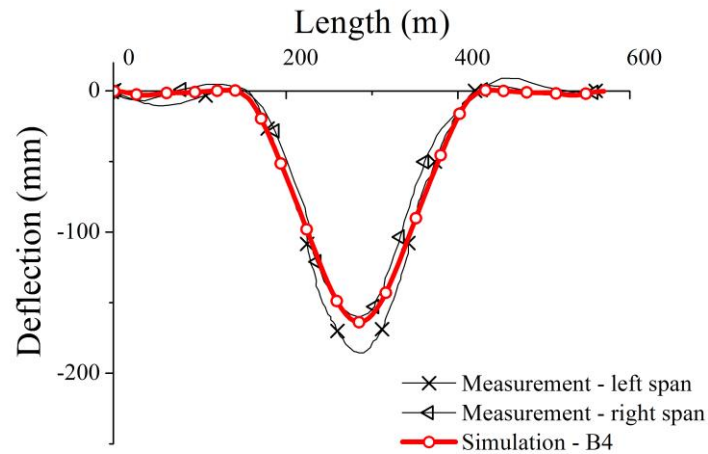


Figure 27. The fourth year profile from the unified model with B4 model and real measurements

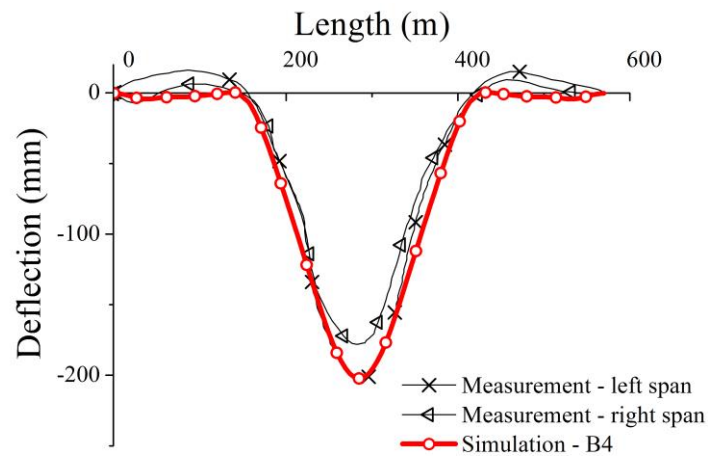


Figure 28. The fifth year profile from the unified model with B4 model and real measurements

6.5 CRACK AND DAMAGE DISTRIBUTION

Concrete cracking is a key element in the unified concrete model to increase the accuracy of the prediction. Therefore, whether the crack and damage distribution match the real situation

is considered in this study. A comprehensive inspection was done to the Humen Bridge at 2003 including the investigation on cracks and damage (Humen Bridge Auxiliary Bridge inspection report, 2011). According to the inspection report, many cracks were founded near the middle span that initiated from the bottom slab and then propagated vertically into the web. Besides, a few skewed cracks were found in the top web area about the $\frac{1}{4}$ span of the main span. The distribution of the cracks at 2003 are illustrated in the Figure 29.

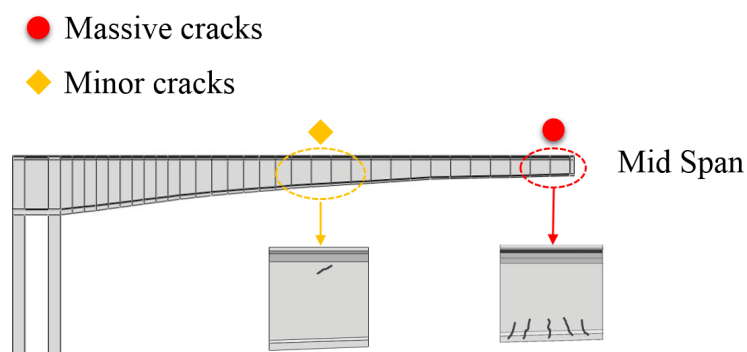


Figure 29. The real crack distribution of Humen Bridge at 2003

Next, the cracks and damage evolution are simulated based on the unified concrete model and the predicting distributions are shown from Figure 30 to Figure 33. After the end of the construction, the strain for the whole bridge is very small and barely any damage can be found. After 1 year, few cracks appear at the bottom slab near to the web at the middle span. Then, by the time of 3 years, these cracks propagate to the whole bottom slab at the middle span. Finally, after the 7 years, the cracks at bottom slab propagate along the longitudinal way, and new small cracks initiate around the $\frac{1}{4}$ span of the main span. Overall, one can find that the simulated cracks and damage evolution match the real one quite well.

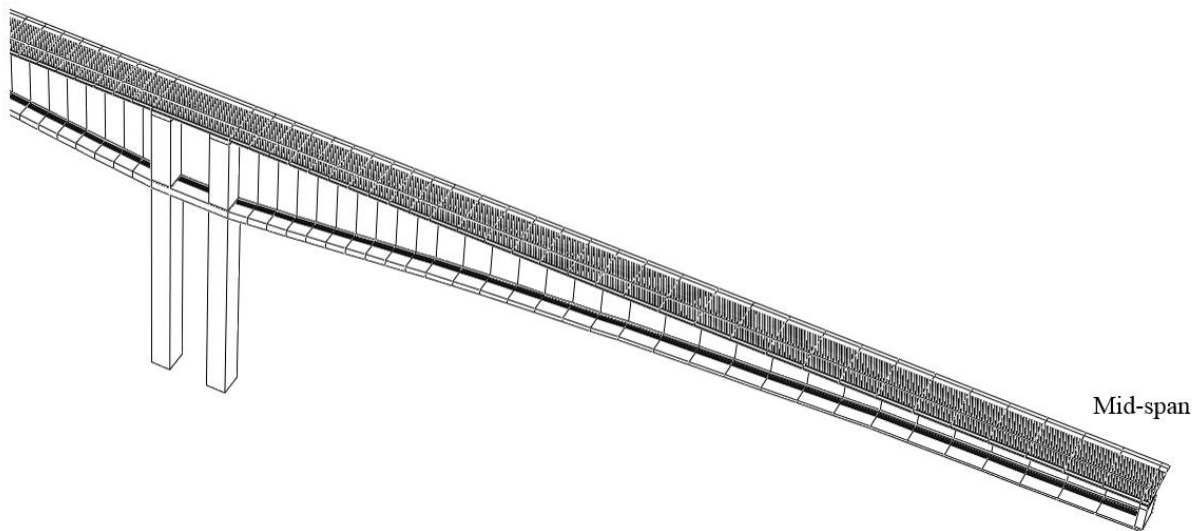


Figure 30. The cracks and damage simulation based on the unified model by the end of construction

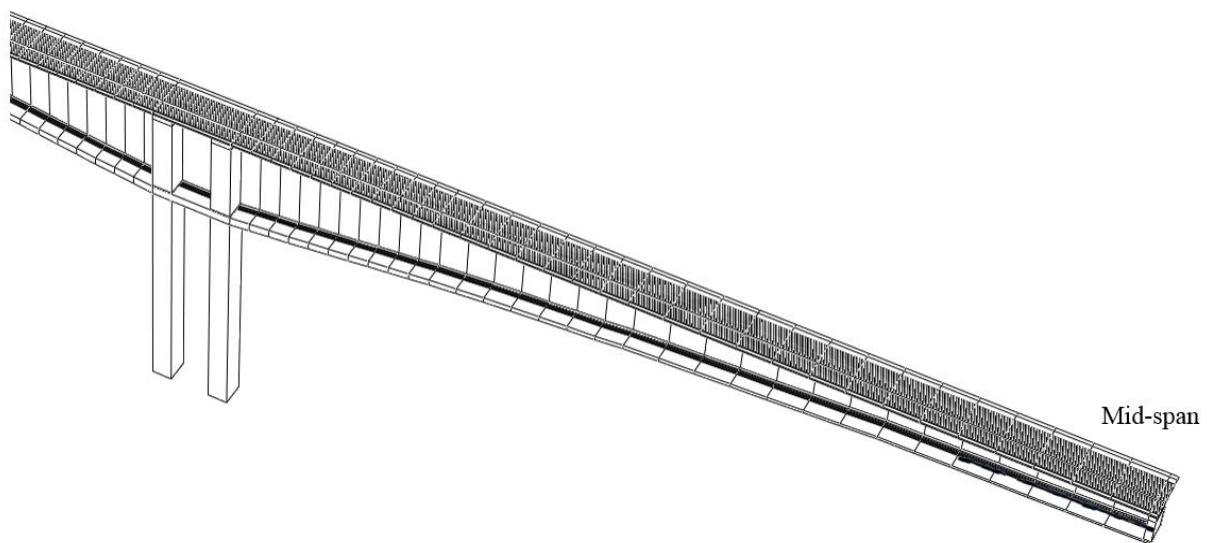


Figure 31. The cracks and damage simulation based on the unified model after 1 year

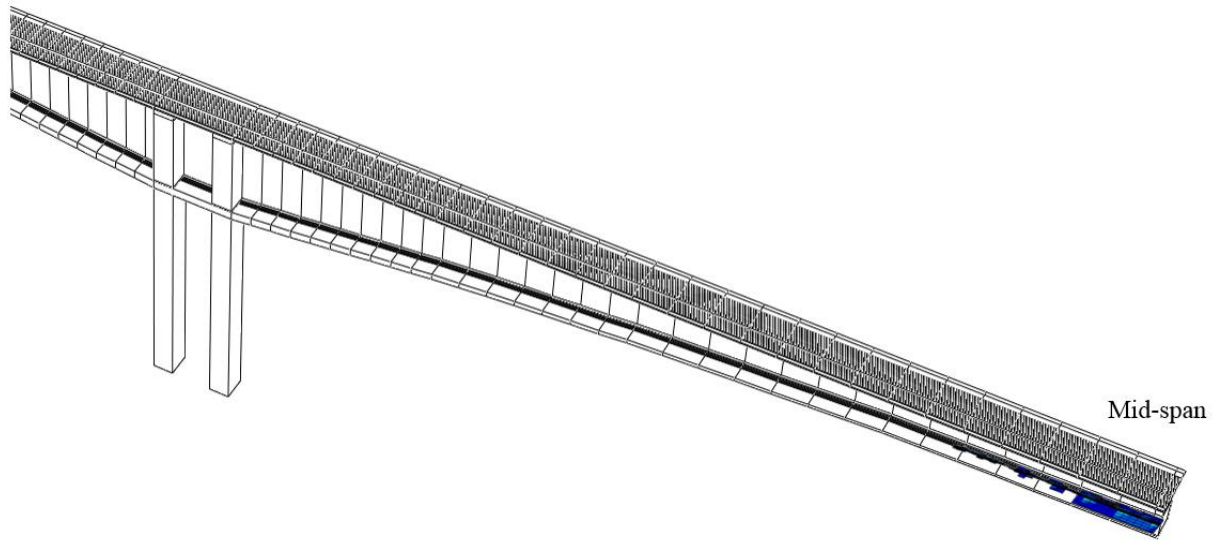


Figure 32. The cracks and damage simulation based on the unified model after 3 years

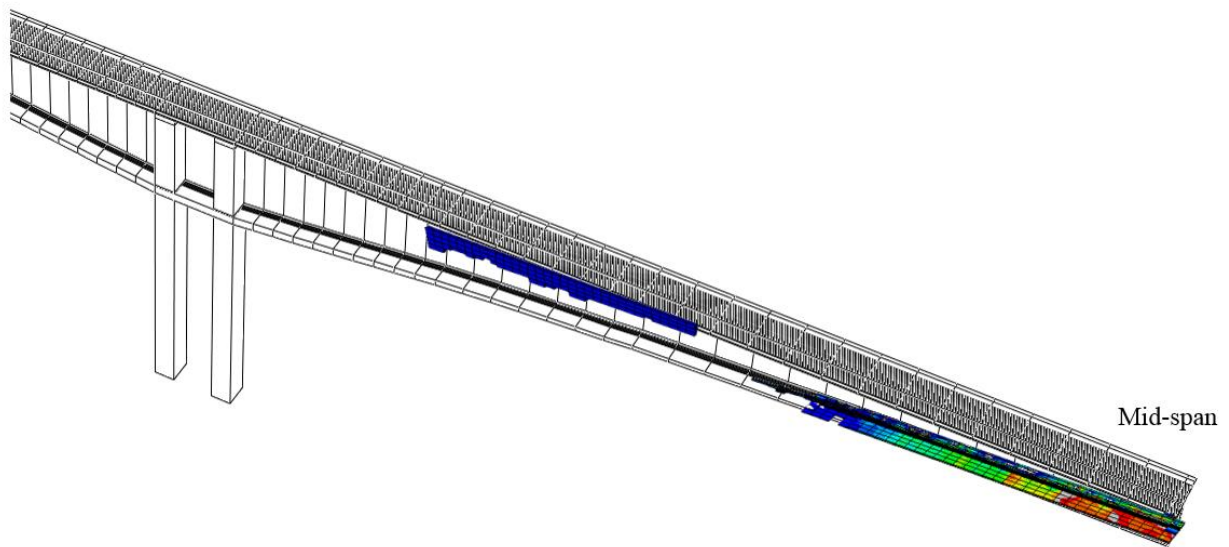


Figure 33. The cracks and damage simulation based on the unified model after 7 years

7.0 CONCLUSION

The pure viscoelastic analysis without considering the cyclic creep and other memory-independent behaviors may not accurately predict the long-term deflection of the the large-span prestressed concrete bridge with heavy traffic flow. Therefore, in this study, a unified concrete model combining the instantaneous behavior (e.g. elasticity, plasticity and damage) with the memory-dependent behavior (e.g. quasi-static and cyclic creep, shrinkage, etc.) is proposed. To demonstrate the effectiveness and advantage of this unified model in predicting the deflection of the large-span prestressed concrete bridge with heavy traffic flow, Humen Bridge, as a case study, is simulated by ABAQUS with rate-type algorithm based on both pure viscoelastic analysis with three creep and shrinkage models (ACI, fib MC2010 and B4 model) and then the unified model with these three models. The simulation results are compared with the real deflections. Based on these results and comparisons, the following conclusions can be drawn:

1. Without considering damage, plasticity and cyclic creep, the pure viscoelastic analysis is insufficient in predicting the deflection of the large-span prestressed concrete bridge carrying heavy traffic flow.

2. In the pure viscoelastic analysis, B4 model gives a more accurate prediction than the other two, while ACI model, totally based on the empirical formulas, gives the least

accurate result. The main reason for this phenomenon is that B4 model divides the creep into basic creep and drying creep with the adjustable parameters which can be updated according to the experiment data and the material used in bridge to match the real deflection.

3. Taking the damage, cyclic creep and other factors in to account, the unified concrete model with suitable parameters whose viscoelastic analysis is based on B4 model can predict the deflection and crack propagation of Humen Bridge quite well.

4. The present investigation may suggest that damage and cyclic creep are critical to accurately predict the large-span prestressed concrete bridge with heavy load like Humen Bridge. Therefore, taking these factors into consideration is a valid way to improve a model in predicting the deflection of the large-span prestressed concrete bridge carrying heavy traffic flow.

5. The successful application of the rate-type implementation with exponential algorithm in the simulation proved the effectiveness of this analysis method. In addition, the efficiency of rate-type algorithm in simulating Humen Bridge, a large scale structure, and the convenience of it in combining the static creep and other effects are well demonstrated in this thesis.

APPENDIX A

CONTINUOUS RETARDATION SPECTRUM

When concrete is under a unit stress applied at time t' , the viscoelastic behavior at current time t is generally characterized by the compliance function $J(t, t')$:

$$J(t, t') = 1/E_0 + C(t, t') \quad (\text{Eq. A-1})$$

where E_0 is the instantaneous elastic modulus; and $C(t, t')$ is the creep part of the compliance function. This $C(t, t')$ can be approximated in a continuous form with $\xi = t - t'$ (Bažant, 1995):

$$C(\xi) \approx \int_0^\infty L(\tau) / \tau (1 - e^{-\xi/\tau}) d\tau = \int_{-\infty}^\infty L(\tau) (1 - e^{-\xi/\tau}) d(\ln \tau) \quad (\text{Eq. A-2})$$

where $L(\tau)$ is defined as the continuous retardation spectrum (Bažant, 1995). To efficiently deduce $L(\tau)$ from the known compliance function, a general method developed by Tschoegl (1971, 1989) is then adopted (Bažant, 1995). Setting $\tau = 1/\zeta$ and $d(\ln \tau) = -d(\zeta)$, Eq. A-2 can be rewritten as (Bažant, 1995):

$$C(\xi) = \int_0^\infty L(\zeta^{-1}) (1 - e^{-\xi\zeta}) \zeta^{-1} d\zeta \quad (\text{Eq. A-3})$$

$$C(\xi) = \int_0^\infty L(\zeta^{-1}) \zeta^{-1} d\zeta - \int_0^\infty \zeta^{-1} L(\zeta^{-1}) e^{-\xi\zeta} d\zeta \quad (\text{Eq. A-4})$$

Then denoting (Bažant, 1995):

$$f(\xi) = \int_0^{\infty} \zeta^{-1} L(\zeta^{-1}) e^{-\xi\zeta} d\zeta \quad (\text{Eq. A-5})$$

one can rewrite Eq. A-4 as:

$$C(\xi) = -f(\xi) + f(0) \quad (\text{Eq. A-6})$$

$f(\xi)$ is the Laplace transform of the function $\zeta^{-1}L(\zeta^{-1})$ and ξ is the transforma variable (Bažant, 1995).

Next, the Laplace transform can be inverted by Widder's inversion formula (Widder, 1971). This inversion formula is expressed as:

$$F_{k,\zeta}[f(\xi)] = \frac{(-1)^k}{k!} \left(\frac{k}{\zeta}\right)^{k+1} f^{(k)}\left(\frac{k}{\zeta}\right) \quad (\text{Eq. A-7})$$

with the property:

$$\lim_{k \rightarrow \infty} F_{k,\zeta}[f(\xi)] = \lim_{k \rightarrow \infty} \left[\frac{(-1)^k}{k!} \left(\frac{k}{\zeta}\right)^{k+1} f^{(k)}\left(\frac{k}{\zeta}\right) \right] = \zeta^{-1} L(\zeta^{-1}) \quad (\text{Eq. A-8})$$

where $f^{(k)}$ is the k th derivative of function f .

Because $f(0)$ is a constant, the continuous retardation spectrum $L(\tau)$ can then be expressed as (Bažant, 1995):

$$L(\tau) = \frac{\lim_{k \rightarrow \infty} (k\tau)^k C^{(k)}(k\tau)}{(k-1)!} \quad (\text{Eq. A-9})$$

APPENDIX B

EXPONENTIAL ALGORITHM

With the application of Kelvin chain model, the constitutive law for creep can be transferred from Volterra integral equations to a system of ordinary first-order linear differential equations (Yu et al., 2012). In this system, the equations for the Kelvin unit strains ε_i can be expressed as (Yu et al., 2012):

$$DD_i(t) \left(\dot{\gamma}_i(t) + \frac{\gamma_i(t)}{\tau_i} \right) = \dot{\sigma}(t) \quad (\text{Eq. B-1})$$

$$\gamma_i(t) = \tau_i \dot{\varepsilon}_i(t) \quad (\text{Eq. B-2})$$

where σ is the 6×1 column stress matrix; ε_i is a 6×1 column matrix represents strains of each Kelvin chain unite; D_i is the elastic moduli for each Kelvin unite; and D is a 6×6 elastic stiffness matrix with a unit value of Young's modulus and expressed as (Yu et al., 2012):

$$D = \frac{1-\nu}{(1+\nu)(1-2\nu)} \begin{pmatrix} 1 & \nu/1-\nu & \nu/1-\nu & 0 & 0 & 0 \\ & 1 & \nu/1-\nu & 0 & 0 & 0 \\ & & 1 & 0 & 0 & 0 \\ & & & \nu^* & 0 & 0 \\ & & & & \nu^* & 0 \\ & & & & & \nu^* \end{pmatrix} \quad (\text{Eq. B-3})$$

where ν is the Poisson ration and $\nu \approx 0.18$ for simplicity; and $\nu^* = (1-2\nu)/(2(1-\nu))$.

The traditional algorithms for this first-order differential equations are stable only if $\Delta t \ll \tau_1$ (τ_1 is the shortest retardation time of Kelvin chain units) (Yu et al., 2012). With the increasing of time step Δt , these traditional algorithms will fail by numerical instability. Therefore, to overcome this problem, the exponential algorithm was developed which is unconditionally stable (Bažant et al., 1971 and 1975, Yu et al., 2012). In this algorithm, two parameters used in the constitutive law are introduced as (Bažant et al., 1971 and 1975, Yu et al., 2012):

$$\beta_i = e^{-\Delta t/\tau_i} \quad (\text{Eq. B-4})$$

$$\lambda_i = \tau_i(1 - \beta_i) / \Delta t \quad (\text{Eq. B-5})$$

BIBLIOGRAPHY

- American Concrete Institute (ACI). (1971). "Prediction of creep, shrinkage and temperature effects in concrete structures." Designing for effects of creep, shrinkage and temperature in concrete structures, ACI, Detroit, 51–93.
- American Concrete Institute Committee. (2008). ACI 209.2 R-08: Guide for Modeling and Calculating Shrinkage and Creep in Hardened Concrete.
- Bažant, Z. P. (1968). On causes of excessive long-time deflections of prestressed concrete bridges. Creep under repeated live load. *Inženýrsk é Stavby*, 16, 317-320.
- Bažant, Z. P. (1971). Numerically stable algorithm with increasing time steps for integral-type aging creep. In *Proc., 1st International Conf. on Structural Mechanics in Reactor Technology*.
- Bažant, Z. P. (1975). Theory of creep and shrinkage in concrete structures: A precis of recent developments. *Mechanics today*, 2, 1-93.
- Bažant, Z. P., & Baweja, S. (2000). Creep and shrinkage prediction model for analysis and design of concrete structures: Model B3. *ACI Special Publications*, 194, 1-84.
- Bažant, Z. P., & Hubler, M. H. (2014). Theory of cyclic creep of concrete based on Paris law for fatigue growth of subcritical microcracks. *Journal of the Mechanics and Physics of Solids*, 63, 187-200.
- Bažant, Z. P., Hubler, M. H., & Yu, Q. (2011). Pervasiveness of Excessive Segmental Bridge Deflections: Wake-Up Call for Creep. *ACI Structural Journal*, 108(6), 766-774.
- Bažant, Z. P., & Panula, L. (1979). Practical prediction of time-dependent deformations of concrete. *Mat ériaux et Construction*, 11(5), 317-328.
- Bažant, Z. P., & Prasannan, S. (1989 a). Solidification theory for concrete creep I: formulation. *Journal of engineering mechanics*, 115(8), 1691-1703.

- Bažant, Z. P., & Prasanna, S. (1989 b). Solidification theory for concrete creep II: verification and application. *Journal of Engineering mechanics*, 115(8), 1704-1725.
- Bažant, Z.P., Wendner, R., & Hubler, M.H. (in press). Model B4 for Concrete Creep including Multi-Decade Prediction: Description and Application. *RILEM – Materials and Structures*.
- Bažant, Z. P., & Xi, Y. (1995). Continuous retardation spectrum for solidification theory of concrete creep. *Journal of Engineering Mechanics*, 121(2), 281-288.
- Bažant, Z. P., Yu, Q., Li, G. H., Klein, G. J., & Kristek, V. (2010). Excessive Deflections of Record-Span Prestressed Box Girder-Lessons learned from the collapse of the Koror-Babeldaob Bridge in Palau. *Concrete International*, 32(6), 44-52.
- Bažant, Z. P., Yu, Q., & Li, G. H. (2012 a). Excessive long-time deflections of prestressed box girders. I: Record-span Bridge in Palau and other paradigms. *Journal of Structural Engineering*, 138(6), 676-686.
- Bažant, Z. K. P., Yu, Q., & Li, G. H. (2012 b). Excessive long-time deflections of prestressed box girders. II: Numerical analysis and lessons learned. *Journal of Structural Engineering*, 138(6), 687-696.
- Castigliano, A. (1873). Th éorie de l'équilibre des systems élastiques (Engineering Degree Thesis). *Politecnico di Torino*, Turin.
- Chen, F. W. and Han, D. J. (1988). Plasticity for structural engineers. *Springer-Verlag*, New York.
- Comité Euro-International du Béton (CEB). (1972). Recommandations internationales pour le calcul et l'exécution des ouvrages en béton: Principes et recommandations, CEB, Paris.
- Fédération Internationale du Béton (2012). *International Federation for Structural Concrete Special Activity Group New Model Code*. Lausanne: International Federation for Structural Concrete.
- Hubler, M.H., Wendner, R., & Bažant, Z.P. (2015). Statistical Justification of Model B4 for Drying and Autogenous Shrinkage of Concrete and Comparisons to Other Models. *RILEM - Materials and Structures*.
- Humen Bridge Auxiliary Bridge inspection report. (2011) Guang dong Humen Bridge Co.,Ltd.

- Jirásek, M., & Bažant, Z. P. (2002). *Inelastic analysis of structures*. New York: John Wiley & Sons.
- La Borderie, C., Mazars, J., & Pijaudier-Cabot, G. (1992). Response of plain and reinforced concrete structures under cyclic loadings. *ACI Special Publication*, 134.
- Lee, J., & Fenves, G. L. (1998). Plastic-damage model for cyclic loading of concrete structures. *Journal of engineering mechanics*, 124(8), 892-900.
- Lublinter, J., Oliver, J., Oller, S., & Onate, E. (1989). A plastic-damage model for concrete. *International Journal of solids and structures*, 25(3), 299-326.
- McDonald, B., Saraf, V., & Ross, B. (2003). A spectacular collapse: Koror-babeldaob (Palau) balanced cantilever prestressed, post-tensioned bridge. *Indian concrete journal*, 77(3), 955-962.
- Menzel, A., Ekh, M., Runesson, K., Steinmann, P. (2005). A framework for multiplicative elastoplasticity with kinematic hardening coupled to anisotropic damage. *Int. J. of Plasticity*, 21, 397–434.
- Ortiz, M. (1985). A constitutive theory for the inelastic behavior of concrete. *Mechanics of materials*, 4(1), 67-93.
- Paris, P. C., and Erdogan, F. (1963). A critical analysis of crack propagation laws. *Journal of Fluids Engineering*.
- Resende, L. (1987). A damage mechanics constitutive theory for the inelastic behaviour of concrete. *Computer methods in applied mechanics and engineering*, 60(1), 57-93.
- Simo, J. & Hughes, T. (1998). *Computational inelasticity*. Springer-Verlag, New York.
- Tada, H., Paris, P. C., & Irvin, G. R. (1973). *The Stress Analysis of Cracks Handbook*. Del Research Corp, Helleitown PA.
- Tao, X. and Phillips, D. V. (2005). A simplified isotropic damage model for concrete under bi-axial stress states". *Cement and Concrete Composites*, 27(6), 716-726.
- Taqieddin, Z. N. (2008). Elasto-plastic and damage modeling of reinforced concrete (Doctoral dissertation).
- Tschoegl, N. W. (1971). A general method for the determination of approximations to the spectral distributions from the transient response functions. *Rheologica Acta*.

- Tschoegl, N. W. (1989). *The phenomenological theory of linear viscoelastic behavior*. Springer-Verlag, Berlin.
- Voyiadjis, G. Z., & Kattan, P. I. (1992). A plasticity-damage theory for large deformation of solids—I. Theoretical formulation. *International Journal of Engineering Science*, 30(9).
- Voyiadjis, G. Z., and Kattan, P. I., (2006). *Advances in Damage Mechanics: Metals and Metal Matrix Composites, with an Introduction to Fabric Tensors*. Second Edition, Elsevier, Oxford.
- Wendner, R., Hubler, M.H., & Bažant, Z.P. (in press a). Statistical Justification of Model B4 for Multi-Decade Concrete Creep and Comparisons to Other Models Using Laboratory and Bridge Databases. *RILEM – Materials and Structures*.
- Wendner, R., Hubler, M.H., & Bažant, Z. P. (in press b). Optimization Method, Choice of Form and Uncertainty Quantification of Model B4 for Concrete Creep and Shrinkage Using Laboratory & Multi-Decade Bridge Databases. *RILEM – Materials and Structures*.
- Widder, D. V. (1971). *An introduction to transform theory*. New York: Academic Press.
- Wu, J. Y., Li, J., & Faria, R. (2006). An energy release rate-based plastic-damage model for concrete. *International Journal of Solids and Structures*, 43(3), 583-612.
- Yu, Q., Bažant, Z. P., & Wendner, R. (2012). Improved Algorithm for Efficient and Realistic Creep Analysis of Large Creep-Sensitive Concrete Structures. *ACI Structural Journal*, 109(5), 665-675.